Canadian Geotechnical Journal

Article

A two-dimensional effective stress framework for modelling whole-life soil strength changes due to pore pressure generation and dissipation, Part 1: Formulation

Y. Wang[a], **C. D. O'Loughlin**[a], **Z. Zhou**[a,b], **and C. Gaudin**[a]

[a]Centre for Offshore Foundation Systems, Oceans Graduate School, University of Western Australia, Perth, WA 6009, Australia; [b]Advanced Modelling, Offshore Energy, Norwegian Geotechnical Institute - NGI, Sandakerveien 140, Oslo, Norway.

Corresponding author: **Zefeng Zhou** (email: zefeng.zhou@ngi.no; zefeng.zhou@uwa.edu.au)

Abstract

The undrained shear strength of contractive fine-grained soils changes with time, reducing due to pore pressure generation and increasing during consolidation. There is an increasing appetite to recognise these temporal soil strength changes in offshore geotechnical design, as it provides a basis for potentially less conservative designs. Contributions to this endeavour are reported across two companion papers. This first paper extends an existing effective stress framework that relates the generation of pore pressure to accumulated plastic shear strain, allowing undrained shear strength to be calculated within the context of critical-state soil mechanics. The main development is the extension of the computational domain to two dimensions, allowing calculations to be made for boundary value problems that cannot be satisfactorily simplified to one-dimensional conditions. The magnitude and distribution of accumulated shear strain surrounding objects buried in soil are quantified through a series of large deformation finite element analyses. These spatial distributions are described using a strain influence function in the new 2D framework to calculate the extent and magnitude of excess pore pressure, and in turn the mobilised soil strength around the buried object. The performance of the 2D framework is examined in the companion paper through retrospective simulations of experimental and numerical data.

Key words: clay, consolidation, cyclic loading, effective stress framework, large-deformation finite element modelling, whole-life soil strength

1. Introduction

The changing strength of the seabed associated with various offshore geotechnical processes has received increasing attention in recent years. The degradation of the strength of fine-grained soils to a residual value, usually induced by large soil deformations during installation processes, can be readily measured in the cyclic remoulding phase of a full-flow penetrometer test (e.g., Randolph et al. 2007; Hodder et al. 2013), whereas the more moderate reductions in soil strength associated with cyclic (operational) loading is typically measured in laboratory element tests (e.g., Andersen 2015). In the periods between load cycles or after installation, soil strength recovers as excess pore pressure dissipates and effective stresses increase. Various studies have considered this strength reduction and recovery process at different scales, including full-flow penetrometer tests (Hodder et al. 2013; Cocjin et al. 2014; Chow et al. 2020; O'Loughlin et al. 2020), laboratory element tests (O'Reilly et al. 1991; Yasuhara and Andersen 1991; Latham et al. 2021), and centrifuge tests of various offshore foundations (Bienen and Cassidy 2013; Cocjin et al. 2014; Vulpe et al. 2014; Zhou et al. 2020*a*). Test data from these studies reveal the range of soil strength that can apply depending on current and previous loading—for example, the penetrometer testing reported in Chow et al. (2020) showed that soil strength can vary by a factor of >20 and underpin the current understanding of whole-life geotechnical design (Gourvenec 2020).

To tackle problems involving large displacements and significant remoulding of gross vertical movements and maintained load, Zhou et al. (2019) developed an effective stress framework that calculates changes in soil strength due to pore pressure generation and dissipation associated with both changing and maintained loads. The framework was established for one-dimensional (1D) problems, such as the vertical penetration of a spudcan into the seabed, which required that the soil domain was discretised as a 1D column or row of soil elements. The foundation was represented as a "point" with triangular influence zones defining the extent and magnitude of shear strain and pore pressure development. Simplified equations were proposed to calculate both the development and dissipation of excess pore pressure induced by shearing and maintained load at each soil element, allowing effective stresses and hence undrained shear strength to be determined. Example profiles of excess pore

pressure and vertical effective stress calculated by the framework are provided in Fig. 1 for the case of spudcan penetration in normally consolidated clay, with an intermediate operating stage. Figure 1 shows that the framework simulates the expected increase in spudcan penetration resistance due to the consolidation-induced strength increases during the operating stage; comparisons with corresponding experimental data are provided in Zhou et al. (2019). Other examples of 1D boundary value problems for which the framework has been applied include changes in plate anchor capacity due to maintained and cyclic loading (Zhou et al. 2020*c*) and changes in riser-seabed stiffness due to repeated vertical motion at the touchdown zone (Zhou et al. 2020*b*).

In some instances, considering the soil response in a single dimension would be an inappropriate idealisation. For instance, suction embedded plate anchors undergo complex movements during the keying process, rotating from the as-installed vertical orientation to an orientation that is close to normal to the mooring chain inclination at the anchor load attachment point. Evidently, the kinematics associated with this process could not be considered within a 1D soil domain. A further example is an embedded mooring chain that adopts an inverse catenary shape in the seabed as the mooring is tensioned, such that the calculation of the geometric configuration and the load taken by the embedded chain is essentially a 2D problem, not to mention the potential spatial and temporal variation in soil strength in the local vicinity of the chain (Sun et al. 2019; Yap et al. 2020). Although spudcan penetration, operation, and extraction can be considered a 1D problem, there is increasing interest in the lateral extent of soil strength changes (Purwana et al. 2005; Gan et al. 2012), as this can potentially influence adjacent structures and affect reinstallation of jack-ups when they return to the site of a previous installation (Kong et al. 2012).

To accommodate the analysis of 2D problems, the existing 1D effective stress framework proposed by Zhou et al. (2019) is extended and implemented within a 2D computational domain. This work is reported across two companion papers that collectively describe the theoretical formulation of the framework and demonstrate its performance. In this first paper, results from large deformation finite-element simulations are used to provide a basis for establishing 2D idealisations of the accumulation of plastic shear strain. These idealisations, together with appropriate vertical stress distributions for maintained load, allow changes in excess pore pressure, effective stress, and undrained shear strength to be calculated from critical-state inspired concepts. The second paper (Wang et al. 2024) explores the potential of the extended 2D framework through a series of simulations for various boundary value problems, which are validated using previously reported experimental data.

2. Large deformation finite element analyses

Before extending the theoretical framework, large deformation finite element (LDFE) analyses were undertaken to understand and quantify the 2D spatial distribution of cumulative plastic shear strain (often referred to as "damage," e.g, see Hodder et al. 2010; Randolph et al. 2012; White et al. 2022) in the soil domain due to continuous penetration. These analyses form the basis for establishing the plastic shear strain influence zones in the extended 2D framework, which is then linked to the excess pore pressure generation and changes in effective stress in Section 3. All analyses were carried out with the commercially available software Abaqus (Dassault Systéms 2014).

2.1. Large deformation finite-element model

The accumulation of "damage" or remoulding in fine-grained soil is often quantified by linking the level of remoulding to the accumulated absolute plastic shear strain (Einav and Randolph 2005). The analytical model developed by Einav and Randolph (2005) has subsequently been applied in finite-element analyses (Zhou and Randolph 2007; Hossain and Randolph 2009) and in theoretical frameworks (Hodder et al. 2009; White and Hodder 2010) to allow for a strain softening response. The LDFE analyses considered in this section explore the distribution and accumulation of plastic shear strains in the 2D domain for two boundary value problems (see Fig. 2, where the coordinate system is defined in terms of $\widehat{x} = \frac{x}{D}$ and $\widehat{z} = \frac{z}{D}$, where x is lateral position, z is depth, and D is the object diameter):

1. Penetration of a cylinder by a vertical displacement, $\widehat{z}$=4 under plane strain conditions.
2. Penetration of a circular plate by a vertical displacement, $\widehat{z}$=4 under axisymmetric conditions.

Case 1 is relevant to undrained penetration of a T-bar penetrometer or a pipeline segment, whereas case 2 simulates the undrained behaviour of vertically loaded plate foundations such as spudcans and plate anchors, with the simplification of reducing their complex geometries to a circular plate with a thickness equal to 0.05 times the diameter, that is, $t_p/D = \widehat{t_p} = 0.05$ (as also considered in the numerical studies of Song et al. (2008), Wang et al. (2010), and Zhang et al. (2012)). Although both cases were idealised as 1D problems in Zhou et al. (2019), it is possible to identify the spatial distribution of accumulated plastic shear strain within the 2D domain and subsequently model the object trajectory when it includes both vertical and lateral components.

In both cases, a displacement of 4D was selected to ensure steady state conditions in which the flow-round failure mechanism forms, and a steady-state pattern of plastic shear strain accumulation can be identified (Zhou and Randolph 2007). Smooth (zero shear stress along interface) and rough (fully bonded interface) interactions were adopted to bound the effect of roughness on the plastic shear strain accumulation. A "no breakaway" (or fully attached) condition is assumed (normal to the interface) due to the potential suction induced by the tensile stress for deeply buried foundations in an undrained condition (Zhang et al. 2012).

Wished-in-place conditions were assumed for both cases, starting with an initial embedment depth of 4D. Only half the model (case 1) or the axisymmetric model (case 2) was consid-

Fig. 1. Analysis procedure of the Zhou et al. (2019) one-dimensional (1D) effective stress framework as applied to spudcan penetration.

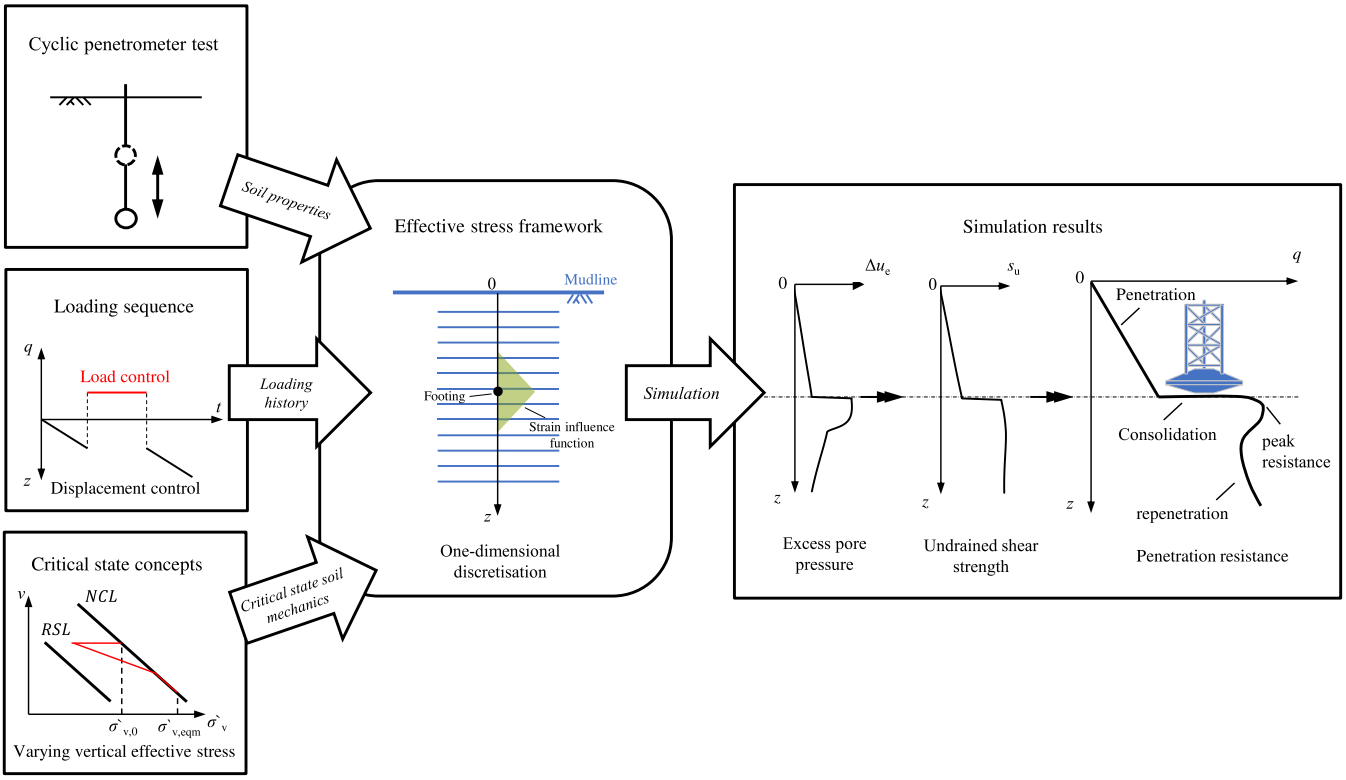

Fig. 2. Large deformation finite element mesh for (*a*) case 1 (cylinder, plane strain) and (*b*) case 2 (circular plate, axisymmetric).

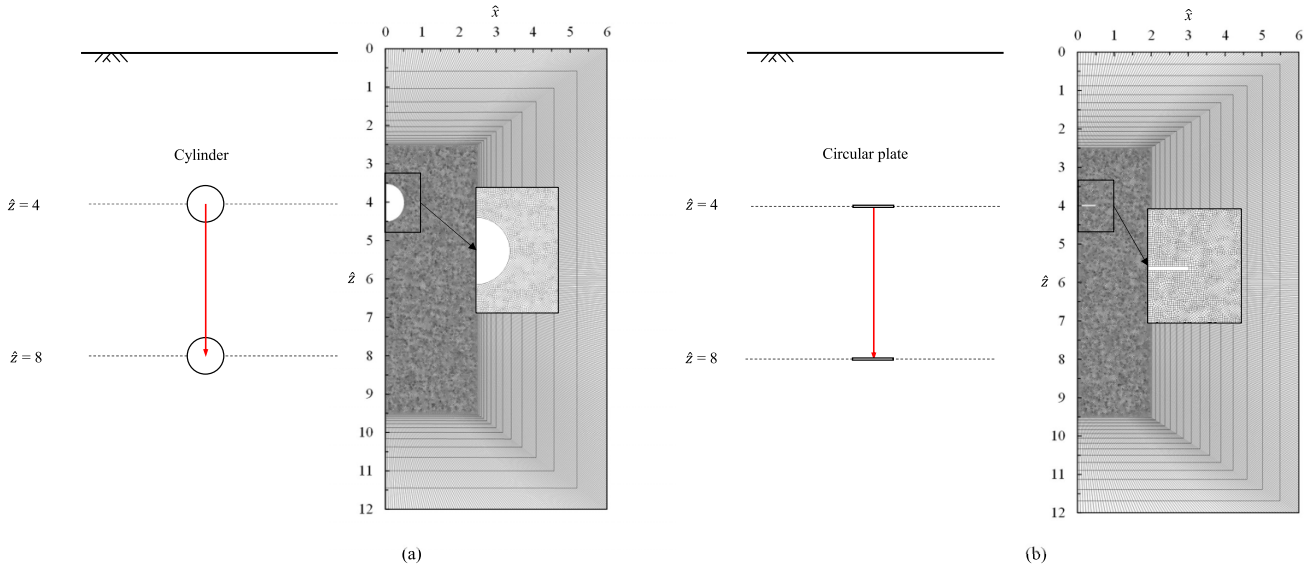

ered to save computational effort (Fig. 2), and the horizontal and vertical extents of the soil mesh were selected as 6D and 12D, respectively, to eliminate boundary effects (Han et al. 2016). The mesh was refined in a zone (see Fig. 2) of height 7D and width of either 2.5D (case 1) or 2D (case 2), where plastic shear strain accumulates around the penetrating object. The minimum element size was 0.02D within this refined zone, increasing to around 1D at the mesh boundaries. Additional trial simulations show that a finer mesh has little effect on the results.

The soil was modelled as an elastic, perfectly plastic Tresca material with uniform undrained shear strength, a constant rigidity index, $E/s_u = 500$, and Poisson's ratio $\nu = 0.49$ (to model undrained conditions). The effective unit weight, γ',

Fig. 3. Comparison of normalised resistance-displacement curves: (*a*) case 1 (cylinder) and (*b*) case 2 (circular plate).

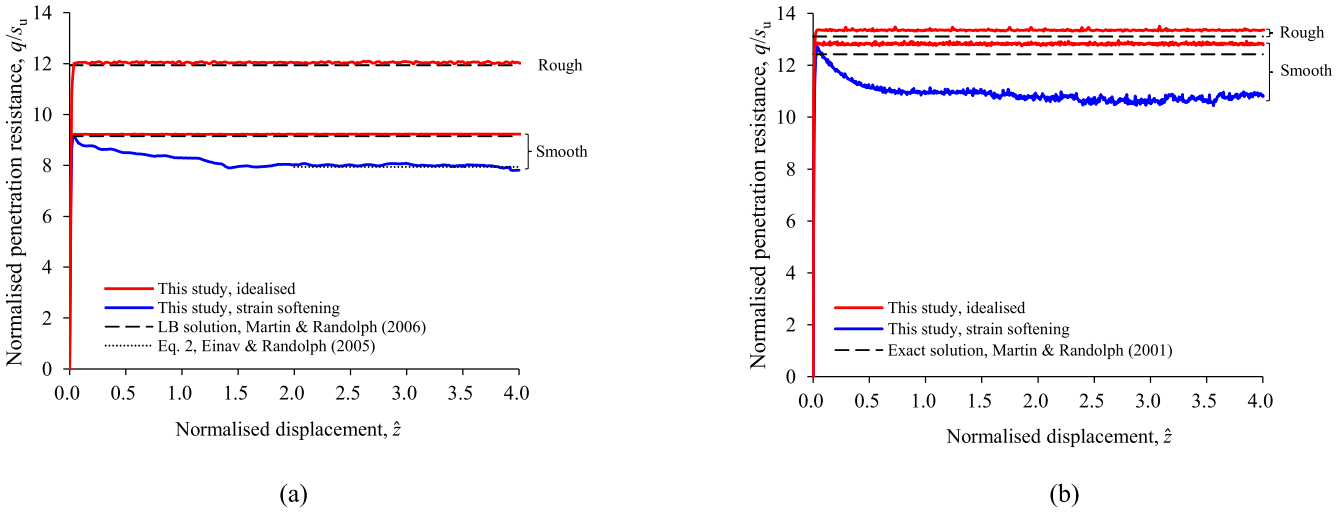

Table 1. Summary of calculated bearing capacity factor, N_c.

	Smooth interface			Rough interface		
Object	N_c (calculated)	N_c (analytical)	Difference (%)	N_c (calculated)	N_c (analytical)	Difference (%)
Cylinder	9.21	9.14	0.8	12.04	11.94	0.8
Circular plate	12.8	12.42	3	13.3	13.11	1.5

was selected to obtain the dimensionless strength term, $s_u/\gamma' D = 0.7$, which is sufficient to ensure that the failure mechanism is deep and localised (Song et al. 2008). To investigate the effect of strain softening on the accumulation of plastic shear strain, two additional strain softening analyses were included for a smooth cylinder and circular plate using the exponential strength softening model of Einav and Randolph (2005):

$$(1) \qquad s_u = s_{u0}\left[\delta_{rem} + (1-\delta_{rem})\, e^{-3\xi/\xi_{95}}\right]$$

where s_{u0} is the initial undrained shear strength prior to any softening, δ_{rem} is the inverse of the soil sensitivity, S_t (taken here as 2.5; Colreavy et al. 2016), ξ is the accumulated absolute plastic shear strain (as discussed later), and ξ_{95} denotes the value of ξ associated with 95% remoulding (taken here as 25, within the range ξ_{95} = 10–50 according to Randolph and Andersen (2006) and Einav and Randolph (2005)). The two soil models considered here are referred to as "idealised" and "softening" for the elastic, perfectly plastic and the strain-softening analyses, respectively.

The simulations adopted the "remeshing and interpolation technique with small strain" approach, originally proposed by Hu and Randolph (1998) and later automated in ABAQUS using a Python script (Tian et al. 2014). Four-node quadrilateral elements (CPE4 for case 1 and CAX4 for case 2) with full integration were adopted to minimise numerical diffusion during mapping of field variables (Roy et al. 2021).

2.2. Results

2.2.1. Validation

The LDFE results are compared with other numerical and analytical solutions in Fig. 3, with penetration resistance, q, normalised by the undrained shear strength (i.e., q/s_u) and vertical displacement normalised by diameter (i.e., $\hat{z}$). The peak calculated normalised resistances (or the bearing capacity factor, N_c) are summarised in Table 1. For case 1 (cylinder), N_c = 9.21 and 12.04 for the smooth and rough interfaces, respectively, which are only 0.8% higher than N_c = 9.14 (smooth) and 11.94 (rough) from the lower bound solution of Martin and Randolph (2006). For case 2 (circular plate), the calculated capacity factors are N_c = 12.8 and 13.3, 3% and 1.5% higher than the exact solutions (N_c = 12.42 and 13.1 for smooth and rough interfaces, respectively; Martin and Randolph 2001) for an ultrathin deeply embedded plate. The slight overestimations of N_c for case 2 are attributed to the thickness ratio, $\hat{t}$ = 0.05, considered in the LDFE analyses and is consistent with other comparisons between plates of finite thicknesses and the zero thickness plate considered by Martin and Randolph (2001) (e.g., Song et al. 2008; Zhang et al. 2012; Wang and O'Loughlin 2014). This level of agreement for both the cylinder and the plate confirms the accuracy of the current LDFE results. The effect of interface roughness on the failure mechanism for both cases is made clear by Fig. 4, which shows contours of the largest principal strain rate, $\dot{\varepsilon}_{max}$, at the mid-depth of penetration ($\hat{z}$ = 6) from the analyses in idealised soil. The left- and right-hand sides of

Fig. 4. Contour plots of the incremental maximum principal shear strain (LHS—smooth interface; RHS—rough interface): (*a*) case 1 (cylinder) and (*b*) case 2 (circular plate). LHS, left hand side; RHS, right hand side.

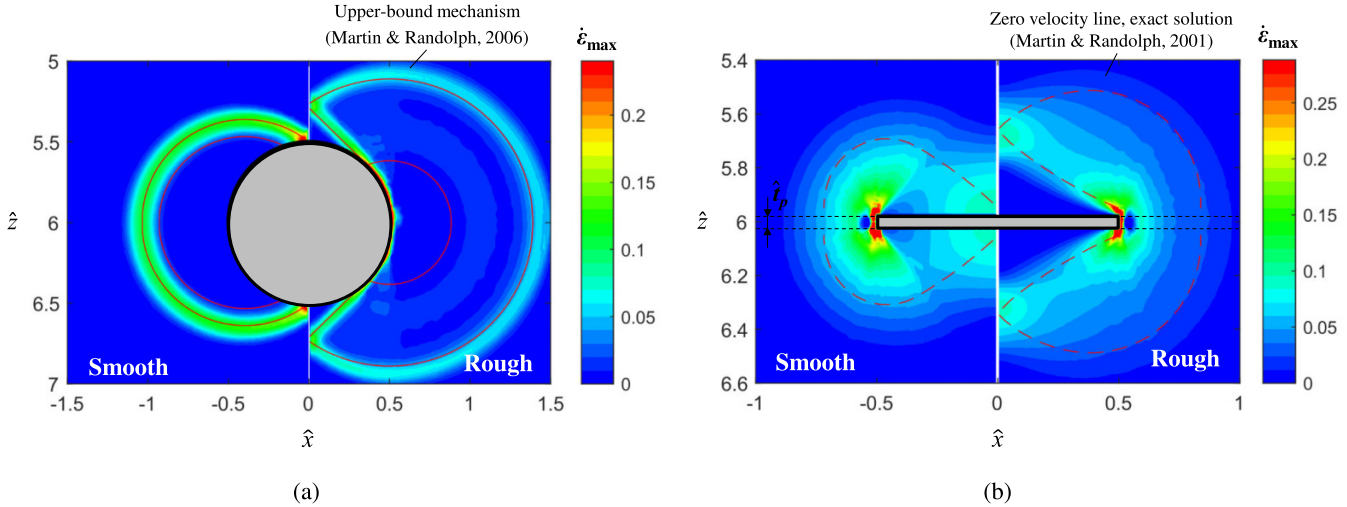

each plot depict results from the smooth and rough interfaces, respectively. Upper bound mechanisms for a cylinder (Martin and Randolph 2006) and the exact solution for an ultrathin plate (Martin and Randolph 2001) are also included in Fig. 4 to provide a basis for examining the validity of the simulation results. In the Martin and Randolph (2006) upper bound mechanism for a cylinder, there are two concentrated velocity discontinuities, denoted in Fig. 4*a* by red solid lines. For a cylinder, the LDFE mechanisms are in good agreement with the upper bound mechanism, albeit that the two distinct shear bands are not evident in the LDFE mechanism for a smooth interface and are subtle for the rough interface. This is consistent with other numerically observed mechanisms (e.g., Sabetamal et al. 2021; Singh et al. 2021) with similar meshes, noting also that the absolute thickness of the shear band reduces with increasing mesh density (Singh et al. 2021). In the mechanism for the circular plate (Fig. 4*b*), the boundary of the mechanism (i.e., at zero velocity) for the Martin and Randolph (2001) exact solution is represented by red dashed lines. As with the cylinder, interface roughness increases the size of the mechanism. This is also captured in the LDFE simulations which are broadly in agreement with the exact solution, noting that the exact solution is for a vanishingly thin plate, whereas the LDFE simulations adopt a plate with a finite thickness.

Figure 3 also includes results from the LDFE simulations that account for strain softening for both a smooth cylinder and a smooth circular plate. These simulations result in a peak normalised penetration resistance that is almost the same as that from the idealised analyses, but that degrades to show residual normalised resistances of $q/s_u = 7.94$ and 10.7 for the cylinder and plate, respectively, when the displacement exceeds ~1.5*D* for the cylinder and ~1.0*D* for the circular plate. Figure 3*a* also shows the empirically determined "softened" bearing capacity factor for a cylinder (Einav and Randolph 2005):

$$(2) \quad N_{c,s} = N_{c,i}\left[\delta_{rem} + (1-\delta_{rem})\, e^{-3\left(\xi_0 + 0.5\xi_p\right)/\xi_{95}}\right]$$

where the bracketed term has a similar form to that in eq.1 and reflects the average strength response due to remoulding, $N_{c,i}$ is the bearing capacity factor for an ideal rigid-plastic material ($N_{c,i} = 9.21$ from the idealised analyses has been adopted here), ξ_0 is the initial strain (taken as zero here as the simulations commence from a wished-in-place condition), ξ_p is the average accumulated plastic shear strain experienced by typical soil elements passing through the failure mechanism, with a suggested value of $\xi_p = 4.42$ for a T-bar with a frictionless interface (Einav and Randolph 2005). The LDFE strain softening result for the cylinder (case 1) is $q/s_u = 7.94$, which is coincident with $N_{c,s}$ calculated using eq. 2, confirming the accuracy of the LDFE strain-softening simulation. Figure 5 compares failure mechanisms (for a smooth interface) for the idealised and strain softening LDFE simulations of both the cylinder and the circular plate. As in Fig. 4, the mechanisms are represented as contours of the largest principal strain rate, $\dot{\varepsilon}_{max}$, at the mid-depth of penetration ($\hat{z} = 6$). As also demonstrated by other numerical studies (Randolph and Andersen 2006; Zhou and Randolph 2007; Singh et al. 2021; Sabetamal et al. 2021), strain softening appears to have limited influence on the failure mechanism, apart from a slight reduction in size and a slight adjustment to the shape (Zhou and Randolph 2007).

2.2.2. Spatial distribution of accumulated plastic shear strain

Einav and Randolph (2005) employed the accumulated absolute plastic shear strain, ξ, to quantify the total amount of distortion undergone by predefined streamlines of soil, defined by

$$(3) \quad \xi = \int_t |\dot{\gamma}_{max}| dt$$

where $\dot{\gamma}_{max}$ denotes the maximum shear strain rate and is determined according to different failure criteria. For the

Fig. 5. Contour plots of the incremental maximum principal shear strain (LHS—no softening; RHS—softening): (*a*) case 1 (cylinder) and (*b*) case 2 (circular plate). LHS, left hand side; RHS, right hand side.

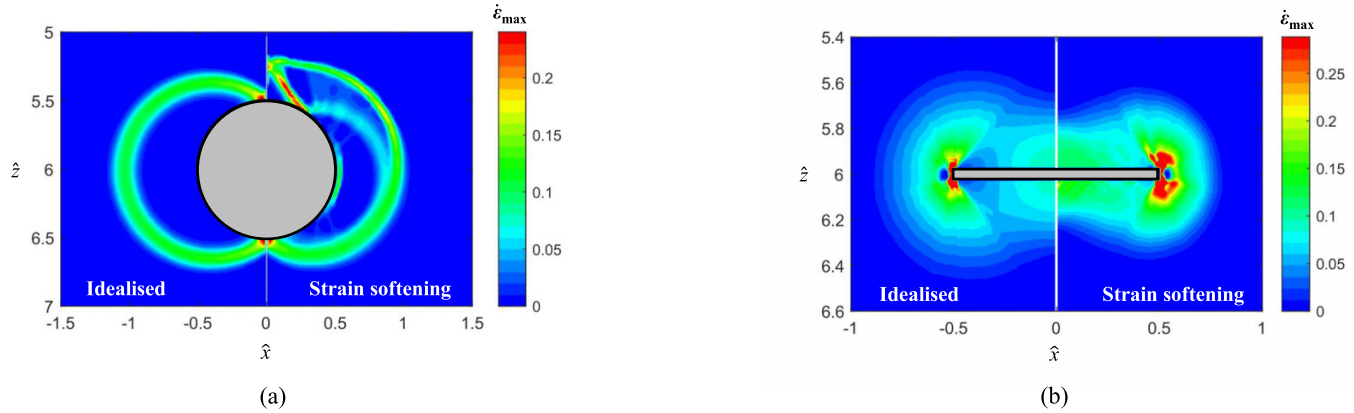

Fig. 6. Contour plots of accumulated plastic shear strain, ξ (LHS—smooth interface; RHS—rough interface): (*a*) case 1 (cylinder) and (*b*) case 2 (circular plate). LHS, left hand side; RHS, right hand side.

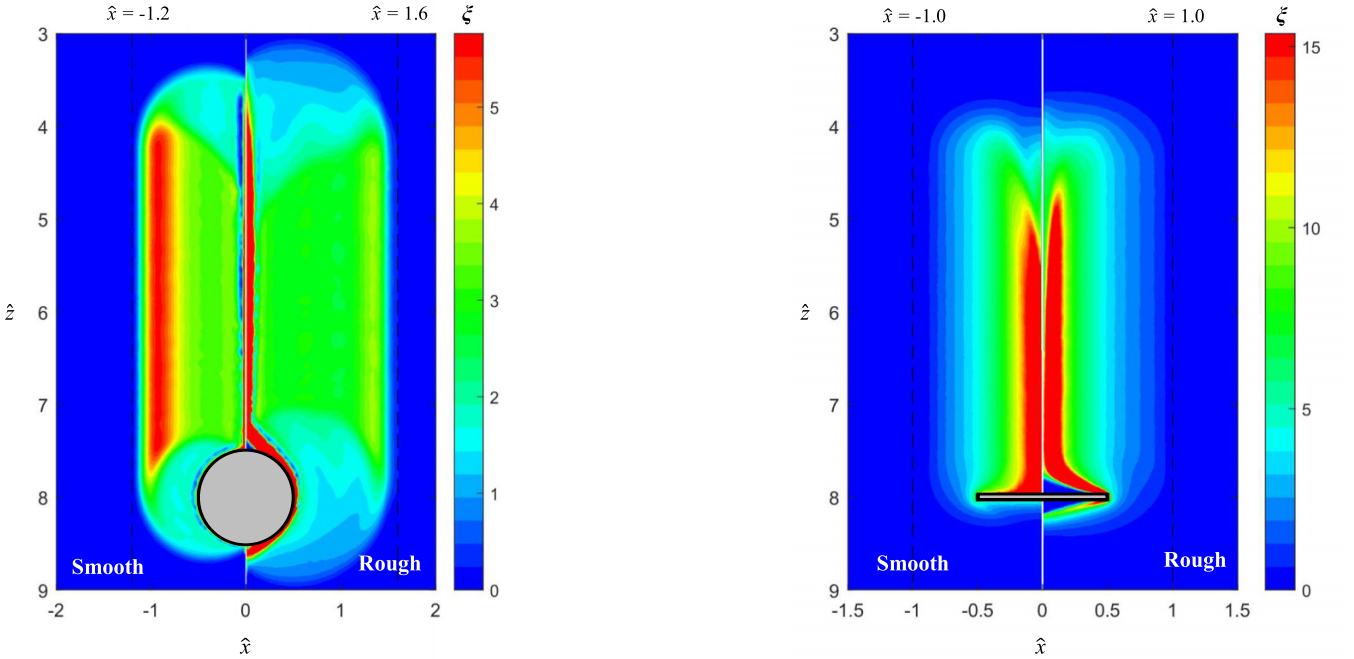

Tresca material used in this study, $\dot{\gamma}_{max} = 2\dot{\varepsilon}_{max}$ is assumed. To explore the spatial distribution of soil disturbance, ξ was tracked throughout the penetration process by following the definition in eq. 3. Instead of establishing streamlines, ξ was calculated and updated at each soil element during the simulation.

Contour plots of ξ from the LDFE idealised simulations considering different interface roughness are provided in Figs. 6*a* and 6*b* for cases 1 and 2, respectively. For the cylinder (case 1), the highest intensity of ξ for a rough interface is around the circumference of the cylinder and along the centreline of the wake of soil behind the advancing cylinder, whereas for a smooth interface, the highest intensity of ξ is at around $\hat{x}$ = 1.0. In the case of a circular plate (case 2), the highest intensity of ξ is along the centreline of the wake of soil, with a clear wedge of immobile (trapped) soil just above and below the rough plate. The lateral extents of the strain accumulation zone (i.e., when $\xi > 0$) for the cylinder are 1.2 and 1.6 times the cylinder diameter for smooth and rough interfaces, respectively. Interface roughness has a much more subtle ef-

Fig. 7. Contour plots of accumulated plastic shear strain, ξ (LHS—no softening; RHS—softening): (*a*) case 1 (cylinder) and (*b*) case 2 (circular plate). LHS, left hand side; RHS, right hand side.

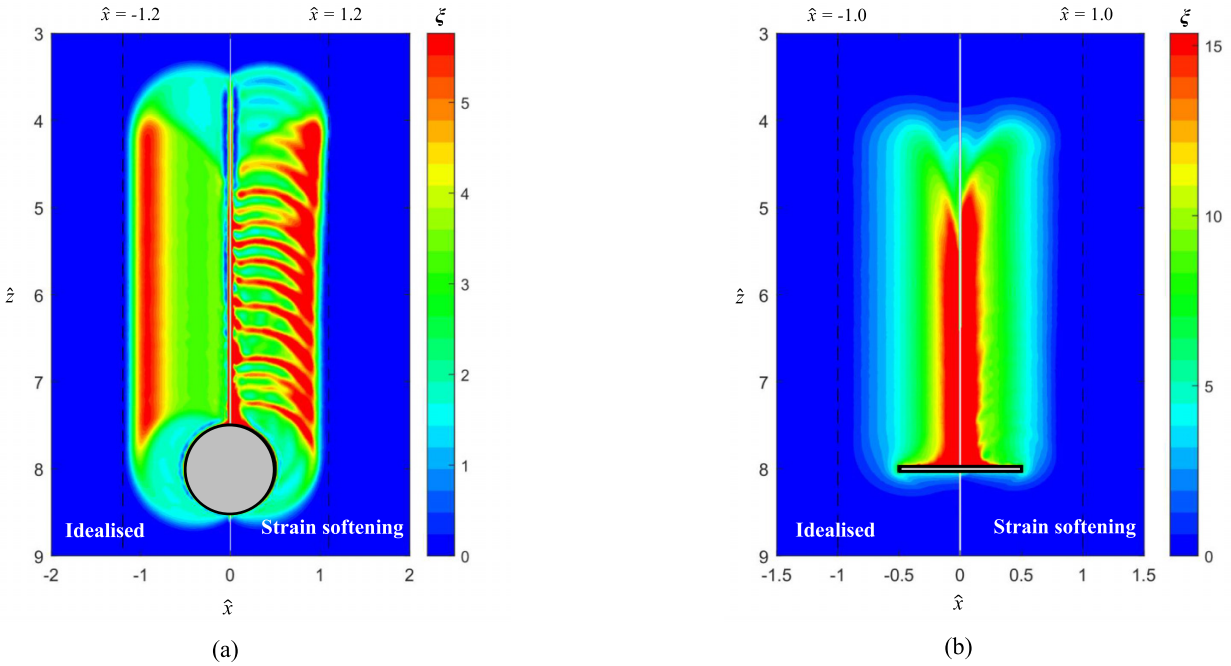

fect for the circular plate, with a lateral extent of the strain accumulation zone equal to approximately the plate diameter for both interfaces.

The effect of strain softening on plastic strain accumulation is demonstrated in Fig. 7 for the cyclinder and circular plate, both with smooth interfaces. Clearly, strain softening leads to periodically forming shear bands during penetration of a cylinder, similar to observations from Zhou and Randolph (2007). However, this periodicity is not evident in the resistance profiles on Fig. 3*a*, potentially because of the choice of ξ_{95}, noting that Zhou and Randolph (2007) did not observe periodic oscillations in the resistance profiles for a cylinder at $\xi_{95} = 25$ (i.e., as also adopted here), but did at $\xi_{95} = 15$ and 10 (albeit that strain-softening was compensated in their simulations by strain rate dependency). In contrast, strain softening does not cause obvious periodic shear banding for a circular plate, with only minor differences in the distribution of ξ between the idealised and strain-softening soils. It is well recognised that implementing strain-softening responses in finite element modelling is difficult due to the mesh dependent strain localisation (e.g., Sluys and De Borst 1992; Zhou and Randolph 2007; Singh et al. 2021). However, an additional circular plate simulation conducted using a mesh twice as fine did not indicate obvious shear banding.

2.3. Integration of accumulated plastic shear strain

Figures 6 and 7 indicate a complex distribution of disturbance in the soil domain. A practical simplification to model the spatially varying ξ is to employ the average concept, by integrating ξ along any direction of interest (Einav and Randolph 2005; Hodder et al. 2010). In this study, ξ is first integrated laterally at each depth to obtain the vertical distribution of accumulated plastic shear strain:

$$(4) \qquad \xi_z(\hat{z}) = \int_{\hat{x}} \xi(\hat{x}, \hat{z})\, d\hat{x}$$

For the horizontal distribution, the value of ξ along a certain soil horizon may be of more interest, or the average accumulated plastic shear strain, $\bar{\xi}$, within a local soil region extending Δz_{ext} above and below the object, that is,

$$(5) \qquad \bar{\xi}(\hat{x}) = \frac{1}{2\Delta\hat{z}_{ext}} \int_{\hat{z}-\Delta\hat{z}_{ext}}^{\hat{z}+\Delta\hat{z}_{ext}} \xi(\hat{x}, \hat{z})\, d\hat{z}$$

2.3.1. Case 1, cylinder

Figure 8*a* shows the profiles of ξ_z calculated by eq. 4 for the cylinder (case 1) with smooth and rough interfaces. For the smooth interface, ξ_z reaches a steady value, denoted as the reference accumulated plastic shear strain, $\xi_{ref} = 9.21$, after a displacement of around one diameter ($\hat{z} = 5$), calculated by (based on Einav and Randolph 2005):

$$(6) \qquad \xi_{ref} = \int_V |\dot{\gamma}_{max}| dV$$

where ξ_{ref} can be considered in the context of energy dissipation, representing the internal energy within the material

Fig. 8. Profiles of accumulated shear strain for case 1 (cylinder): (*a*) vertical profiles and (*b*) horizontal profiles.

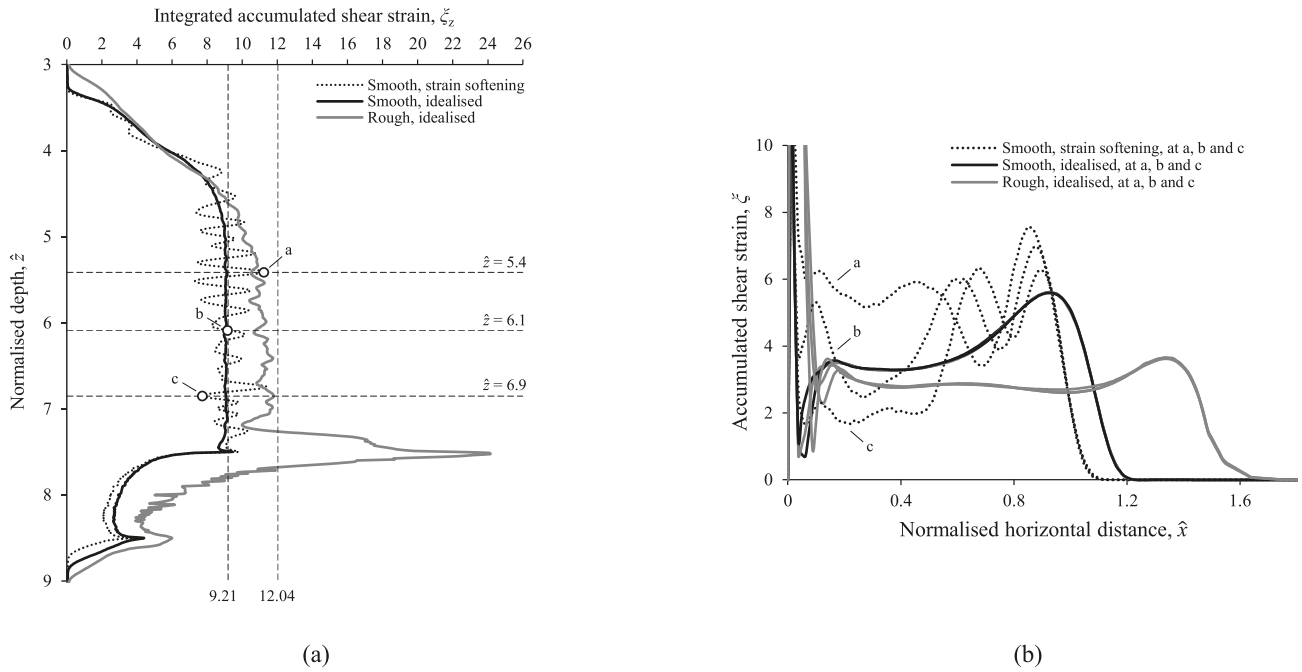

(a) (b)

due to soil element deformation. ξ_{ref} is identical to the LDFE determined N_c reported earlier, as no energy is dissipated along fully smooth and rough interfaces (based on Einav and Randolph 2005), such that:

$$\xi_{ref} = N_c \quad (7)$$

Figure 8*a* also includes the profile of ξ_z for a strain softening soil, which also tends towards a similar average ξ_{ref} value, but with fluctuations associated with the shear banding.

For the rough interface, ξ_z increases over the first 1.5 diameters (i.e., up to $\hat{z} = 5.5$) before becoming tolerably steady in the range ξ_z = 10.4–11.7 over $\hat{z}$ = 5.5–7.0, lower than the LDFE determined N_c = 12.04 (and hence ξ_{ref} in eq. 7) between $\hat{z}$ = 5 and 7.2, but with a localised increase (>12.04) between $\hat{z}$ = 7.2 and 7.7 at the final penetration depth, $\hat{z}$ = 8. According to eqs. 6 and 7, the integration of ξ_z (i.e., the area enclosed by ξ_z on Fig. 8*a*) divided by the total normalised penetration depth ($\Delta\hat{z} = 4$) should match ξ_{ref} = 12.04 according to eqs. 6 and 7. The calculated value for the smooth interface yields 9.6, 4.2% higher than ξ_z = 9.21, whereas for the rough case, the equivalent value is 12.52, 4.0% higher than ξ_z = 12.04. Hence, the differences are negligible for both interfaces and are mainly due to accumulated numerical errors during the interpolation and mapping process using the built-in linear interpolation technique in ABAQUS.

To demonstrate the lateral distribution of ξ, profiles at selected soil horizons beyond a full diameter of penetration are considered (at a, b, and c in Fig. 8*a*). These soil horizons were chosen to investigate potential differences in the lateral distribution of ξ for the strain softening case, noting that points a and c represent the highest and lowest values of ξ_z, while point b was selected to coincide with the same magnitude of ξ_z in the idealised case. The lateral profiles are shown in Fig. 8*b*, where it is clear that the strain softening profiles vary for $\hat{x} \leq 0.9$ associated with lateral "movement" through the shear bands, but then converge to a single response beyond the lateral extent of the shear banding (see Fig. 8*a*), reducing to zero at the lateral extent of the failure mechanism at $\hat{x}$ = 1.1. The lateral profiles for the smooth cylinder in idealised soil are essentially identical for each of the depths at a, b, and c, as no periodic shear bands develop within the disturbed soil, and differ slightly from the softening case, reducing to zero at $\hat{x}$ = 1.2, indicating a slightly wider mechanism for the non-softening case (as also shown by Fig. 3). Profiles for the rough cylinder in idealised soil at each of the three depths considered are also essentially identical as these analyses also ignore strain softening. These are similar to those of the smooth cylinder (in idealised soil), albeit that the average value of ξ is lower and plastic shear strain accumulates over a wider later extent, around 1.6 times the cylinder diameter, consistent with the wider failure mechanism for the rough interface (see Fig. 6*a*).

2.3.2. Case 2, circular plate

A similar analysis was undertaken for case 2. However, as the penetration of a circular plate (case 2) is essentially an asymmetric stress problem, it becomes important to resolve the 3D mesh onto a 2D plane. This is achieved by firstly revolving the asymmetric mesh though 360° (around the $\hat{z}$ axis) to form a 3D model with the same mesh size, with ξ mapped to each node of the 3D mesh (similar to the approach adopted in previous finite-element studies, e.g., Zhang et al. (2014) and Ragni et al. (2016)). Second, the distribution of ξ in the

Fig. 9. Scheme of revolving and mapping, and integration processes to obtain two-dimensional (2D) distribution of accumulated shear strain for case 2 (circular plate).

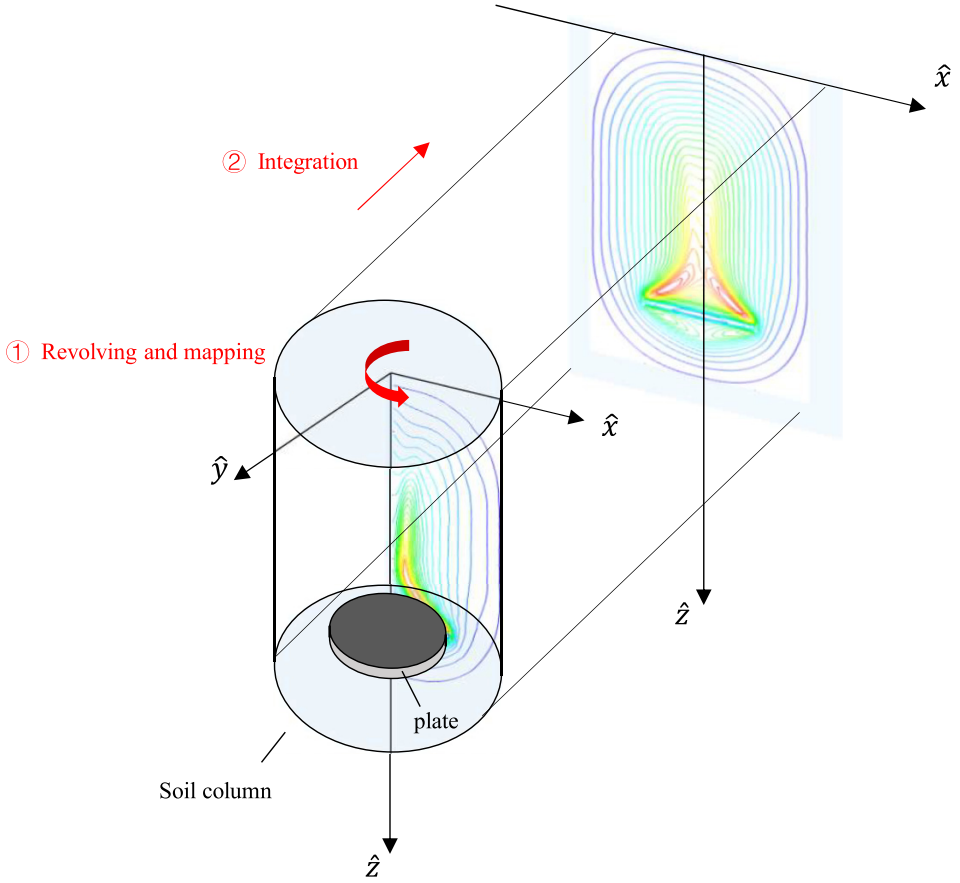

2D domain is obtained by integrating ξ along the $\hat{y}$ axis and projecting onto the $\hat{x}$-$\hat{z}$ domain. The scheme is illustrated in Fig. 9.

Figure 10*a* shows the profiles of ξ_z for case 2, established from eq. 4 together with the reference accumulated plastic shear strain, $\xi_{ref} = 6.4$ and 6.65 for smooth and rough cases, respectively. The value of ξ_{ref} for the asymmetric case is calculated by eq. 8, which is based on theoretical analysis of ball penetration (Einav and Randolph 2005) and expressed as:

$$\xi_{ref} = \frac{\int_V |\dot{\gamma}_{max}| dV}{\hat{w}} \quad (8)$$

where ξ_{ref} has the same physical meanings as in eq. 6, and $\hat{w}$ is the normalised width of the disturbed zone, taken as 2.0 in this study (see Figs. 6*b*, 7*b*, 10*b*, and 10*c*). As noted earlier, for the smooth and rough interfaces considered here, the internal dissipation of energy along the interface is zero such that eq. 8 becomes:

$$\xi_{ref} = \frac{N_c}{\hat{w}} \quad (9)$$

Figure 10*a* indicates that the ξ_z profiles are independent of the different interface conditions and softening response, ξ_z, and reach a steady state $\xi_{ref} = 6.4$ after about 1.5 diameters. As with the cylinder (see Fig. 8), trapped soil above the plate anchor causes a localised peak in accumulated plastic shear strain at $\hat{z} = 7.9$ (i.e., towards the end of anchor movement), reaching $\xi_z = 11$. This localised increase initiates at around $\hat{z} = 7.5$ for the rough interface and at around $\hat{z} = 7.7$ for the smooth interface, with no discernible difference in the idealised and strain softening responses (for the smooth interface). The earlier initiation for the rough interface is attributed to the volume of trapped soil above the plate, as demonstrated by the contour plots of accumulated plastic shear strain in Fig. 6*b*.

To explore the lateral distribution of accumulated plastic shear strain for a circular plate, Fig. 10 also shows the lateral profiles of ξ at the mid-depth of penetration ($\hat{z} = 6$, Fig. 10*b*) and the average integrated accumulated plastic shear strain, $\bar{\xi}$, over a localised zone $\Delta\hat{z}_{ext} = \pm 0.5$ at $\hat{z} = 8$ (Fig. 10*c*). Evidently, Fig. 10*b* is relevant when the response in the zone of softened soil in the wake of the displaced plate is of interest, whereas Fig. 10*c* pertains to the soil response in the immediate vicinity of the plate, which is of interest when the capacity of the plate is under consideration.

Fig. 10. Profiles of accumulated shear strain for case 2 (circular plate): (*a*) vertical profiles, (*b*) horizontal profile at depth of $\hat{z} = 6$, and (*c*) horizontal profiles within a localised zone at $\hat{z} = 8 \pm \Delta\hat{z}_{ext}$.

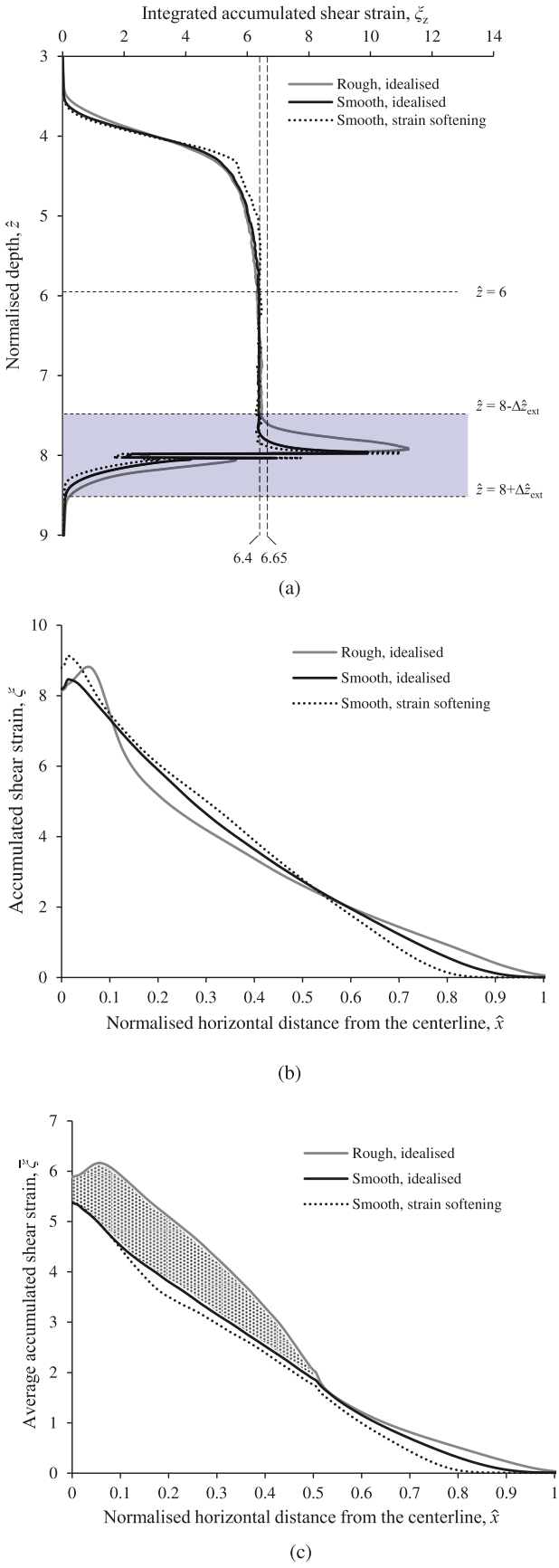

Figure 10*b* shows only minor differences in the lateral distributions of ξ at $\hat{z} = 6$ for the two interface conditions and when soil softening is and is not considered. The lateral extent over which plastic shear strain accumulates is slightly lower for the smooth interface than the rough interface, and slightly lower for a softening soil ($\hat{x} = 0.85$) than for an idealised soil ($\hat{x} = 1$). As noted earlier in the paper, this differs considerably from the distributions for a cylinder (see Fig. 8), for which both the interface and the softening response have a distinct effect on the distribution of accumulated shear strain.

Consistent with the lack of shear banding shown in Fig. 7*b* for the circular plate, the profiles for the smooth interface with and without softening in Fig. 11*c* are similar and decay with lateral distance in the same manner as at $\hat{z} = 6$ (Fig. 10*b*). In contrast, $\bar{\xi}$ is higher for the rough interface up to the edge of the plate (i.e., $\hat{x} \leq 0.5$). The enclosed area between the smooth and rough profiles indicates the amount of accumulated shear strain within the trapped soil above and beneath the plate and is approximately $\xi = 0.98$ for the localised zone defined by $\Delta\hat{z}_{ext} = \pm 0.5$. According to Einav and Randolph (2005) and Zhou et al. (2019), ξ_{ref} represents the average accumulated shear strain of a soil element at a given soil horizon after a full passage of a penetrating object. Therefore, the difference in the gross amount of accumulated shear strain induced by the motions of objects with smooth and rough interfaces can be calculated as $\xi = (6.65 - 6.4) \times 4 = 1.0$, which is essentially identical to $\xi = 0.98$ given by the enclosed area in Fig. 10*c*. This indicates that the rough interface of the plate only causes accumulation and concentrations of accumulated shear strain around the plate due to the trapped soil but has minimal effect on the softened zone of soil in the wake of the plate.

3. An effective stress framework for 2D analyses

3.1. Overview

Results from the LDFE simulations provide insight into the spatial variation of accumulated plastic shear strain, which forms the basis for extension of the effective stress framework, accounting for changes in soil state (e.g., excess pore pressure, vertical effective stress, void ratio) in a 2D domain. This section introduces the components and analysis procedure of the framework, while the following section provides details of how the framework is extended relative to the original critical-state based framework (Zhou et al. 2019).

Figure 11*a* shows the nomenclature and sign convention adopted here. As introduced earlier in the paper, $\hat{x}$ and $\hat{z}$ are normalised distances used to establish the 2D coordinate system, such that generalised object movements can be made by prescribing displacement increments in any direction through a combination of $d\hat{x}$ (horizontal increments) and $d\hat{z}$ (vertical increments). $\hat{x}_c$ and $\hat{z}_c$ denote the current coordinates of the object centroid. A 2D strain influence zone is defined to specify the mobile zone that is moving with

Fig. 11. Schematic representation of analysis procedure.

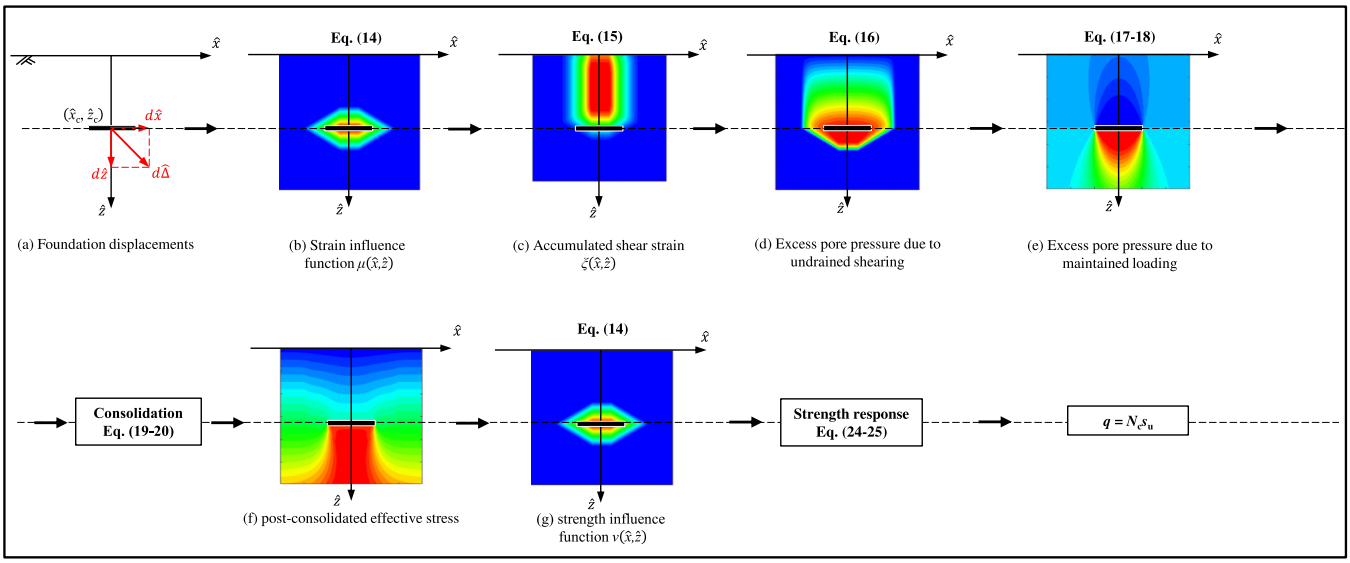

Fig. 12. A critical-state-based interpretation of vertical effective stress paths for undrained shearing and reconsolidation processes (after Zhou et al. 2019).

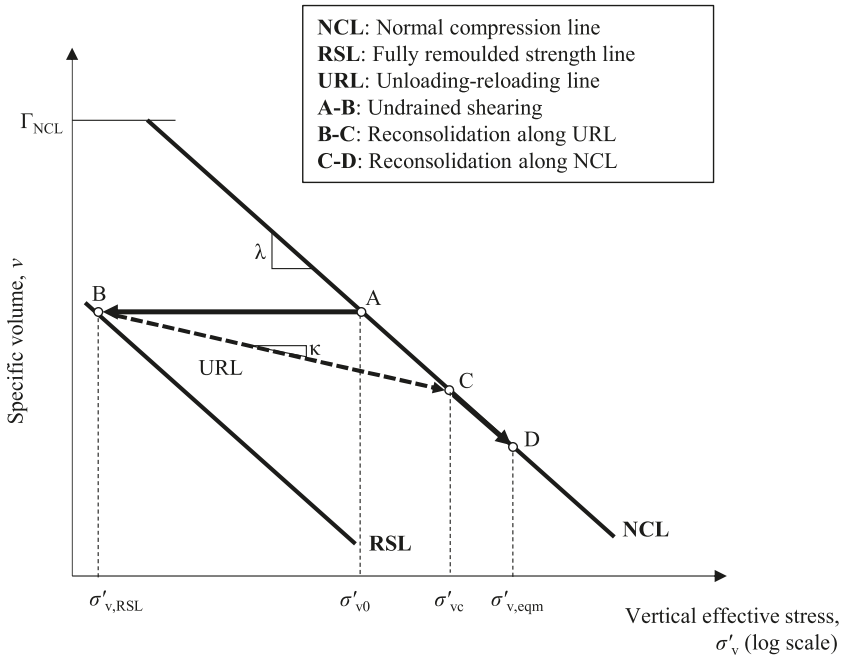

the object, within which shear strains accumulate. The reference accumulated plastic shear strain, ξ_{ref}, from the LDFE simulations is then adopted to describe the gross accumulated shear strain experienced by a given soil horizon for a full passage of an object into and out of the influence zone. The value of ξ_{ref} can be obtained by using the appropriate normalised resistance factor according to eqs. 7 and 9.

The components and analysis procedure of the framework are presented in Fig. 11, which follows the same concepts as the original Zhou et al. (2019) framework, but with extensions to a 2D domain, which required the definition of an appropriate 2D strain influence zone. A strain influence function, $\mu(\hat{x},\hat{z})$, is then defined to calculate the incremental shear strain, $d\xi(\hat{x},\hat{z})$, in the vicinity of the object due to the incremental displacement, $d\hat{\delta}$ (e.g., movement along the vertical direction as shown in Fig. 11*b*). Integration of incremental shear strain over the influence zone yields the reference accumulated shear strain, ξ_{ref}. As the object displaces within the soil domain, $\xi(\hat{x},\hat{z})$ accumulates according to the strain influence function (Fig. 11*c*). Meanwhile, shearing-induced excess pore pressure, denoted as $u_e(\hat{x},\hat{z})$, is generated in a rate-dependent form according to the shear strain rate $d\xi(\hat{x},\hat{z})$, leading to a reduction in vertical effective

Table 2. Components and equations of framework.

Modules	Components	Sign	Equations	Equation No.
Initial state	In situ geostatic effective stress	$\sigma'_{v,0}(\hat{x},\hat{z})$	$\sigma'_v(\hat{x},\hat{z}) = \gamma\hat{z}$	(10)
	Initial specific volume	$v_i(\hat{x},\hat{z})$	$v_i(\hat{x},\hat{z}) = \Gamma_{NCL} - \lambda \mathrm{In}[\mathrm{OCR}(\hat{x},\hat{z})\,\sigma'_{v,0}(\hat{x},\hat{z})] + \kappa \mathrm{In}[\mathrm{OCR}(\hat{x},\hat{z})]$	(11)
	Effective stress on normal consolidation line (NCL)	$\sigma'_{v,NCL}(\hat{x},\hat{z})$	$\sigma'_{v,NCL}(\hat{x},\hat{z}) = exp\left(-\frac{\Gamma_{NCL}-v(\hat{x},\hat{z})}{\lambda}\right)$	(12)
	Effective stress on remoulded strength line (RSL)	$\sigma'_{v,RSL}(\hat{x},\hat{z})$	$\sigma'_{v,RSL}(\hat{x},\hat{z}) = \left[\frac{s_u}{\sigma'_{v,0}}\right]_{NC}\frac{\sigma'_{v,0}(\hat{x},\hat{z})}{\Phi_{steady}S_t}\, exp\left(\frac{\Lambda\left[\Gamma_{NCL}-v_i(\hat{x},\hat{z})-\lambda \mathrm{In}\left[\sigma'_{v,0}(\hat{x},\hat{z})\right]\right]}{\lambda-\kappa}\right)$	(13)
Undrained loading process	Strain influence function	$\mu(\hat{x},\hat{z})$	$\mu(\hat{x},\hat{z}) = h\begin{cases}1, & \lvert\hat{x}\rvert \le \beta_w,\ \lvert\hat{z}\rvert \le \beta_h\\ 1-\frac{\lvert\hat{z}\rvert-\beta_h}{\alpha_h-\beta_h}, & \lvert\hat{x}\rvert \le \beta_w,\ \lvert\hat{z}\rvert \ge \beta_h\\ 1-\frac{\lvert\hat{x}\rvert-\beta_h}{\alpha_w-\beta_w}, & \lvert\hat{x}\rvert \ge \beta_w,\ \lvert\hat{z}\rvert \le \beta_h\\ 1-\frac{\lvert\hat{z}\rvert-\beta_h}{\alpha_h-\beta_h}-\frac{\lvert\hat{x}\rvert-\beta_h}{\alpha_w-\beta_w}, & \lvert\hat{x}\rvert \ge \beta_w,\ \lvert\hat{z}\rvert \ge \beta_h\end{cases}$ where $h = \frac{1}{4\beta_w\beta_h+2\beta_w(\alpha_h-\beta_h)+2\beta_h(\alpha_w-\beta_w)+\frac{2}{3}(\alpha_w-\beta_w)(\alpha_h-\beta_h)}$	(14)
	Incremental accumulated shear strain	$d\varepsilon(\hat{x},\hat{z})$	$d\xi(\hat{x},\hat{z}) = \xi_{ref}\cdot\mu(\hat{x},\hat{z})\,d\hat{\Delta}$	(15)
	Excess pore pressure generation due to undrained shearing	$\delta u_e(\hat{x},\hat{z})$	$\frac{\delta u_e(\hat{x},\hat{z})}{\delta\xi(\hat{x},\hat{z})} = \frac{\chi}{\xi_{99}}\left[\frac{\sigma'_v(\hat{x},\hat{z})-\sigma'_{v,RSL}(\hat{x},\hat{z})}{\sigma'_{v,NCL}(\hat{x},\hat{z})-\sigma'_{v,RSL}(\hat{x},\hat{z})}\right]^p$	(16)
Maintained loading	Stress distribution factor	$u_e(\hat{x},\hat{z})$	$\Delta u_e(\hat{x},\hat{z}) = \begin{cases}\left(\frac{1-sign(v_p)}{2}-\eta\right)\left[\frac{6}{\pi}\iint_{\mathbb{R}} Q(\mathbb{R})\frac{(\hat{z}_c-\hat{z})^3}{\left[4\hat{x}^2+(\hat{z}-\hat{z}_c)^2\right]^{\frac{5}{2}}}d\mathbb{R}\right], & \hat{z} < \hat{z}_c\\ \left(\frac{1+sign(v_p)}{2}-\eta\right)\left[\frac{6}{\pi}\iint_{\mathbb{R}} Q(\mathbb{R})\frac{(\hat{z}-\hat{z}_c)^3}{\left[4\hat{x}^2+(\hat{z}-\hat{z}_c)^2\right]^{\frac{5}{2}}}d\mathbb{R}\right], & \hat{z} \ge \hat{z}_c\end{cases}$	(17)
Consolidation process	Excess pore pressure dissipation due to consolidation	$\delta u_e(\hat{x},\hat{z})$	$\frac{\delta u_e(\hat{x},\hat{z})}{\delta t} = -\frac{u_{e,i}(\hat{x},\hat{z},t)\cdot c_v{}^m\cdot t^{m-1}\cdot(D^2T_{50})^m\cdot m}{\left[(D^2T_{50})^m+(c_v t)^m\right]^2}$	(19)
	Changes in specific volume	$\Delta v(\hat{x},\hat{z})$	$\Delta v(\hat{x},\hat{z}) = -\kappa \mathrm{In}\left[\frac{\sigma'_{vc}(\hat{x},\hat{z})}{\sigma'_v(\hat{x},\hat{z})}\right] - \lambda \mathrm{In}\left[\frac{\sigma'_v(\hat{x},\hat{z})+\Delta\sigma'_v(\hat{x},\hat{z})}{\sigma'_{vc}(\hat{x},\hat{z})}\right]$	(20)
Strength response	Lumped strength parameter	Φ	$\Phi(\hat{x},\hat{z}) = \left\{[\mathrm{OCR}(\hat{x},\hat{z})]^b\text{-}1\right\}\Phi_{steady}\text{-}\left\{[\mathrm{OCR}(\hat{x},\hat{z})]^b\text{-}1\right\}\left[1\text{-}e^{-3\xi(\hat{x},\hat{z})/\xi_{95,\Phi}}\right]\Phi_{steady}$	(21)
	Undrained shear strength	$s_u(\hat{x},\hat{z})$	$s_u(\hat{x},\hat{z}) = \Phi\sigma'_v(\hat{x},\hat{z})$	(22)
	Averaged undrained shear strength	$s_{u,av}$	$s_{u,av} = \int_V s_u(\hat{x},\hat{z})\cdot v_s(\hat{x},\hat{z})\,dV$	(23)
	Mobilised undrained shear strength	$s_{u,mob}$	$\delta\left(\frac{s_{u,mob}}{s_{u,av}}\right) = \delta(\hat{x},\hat{z})\,K$	(24)
			$K = \left\{\left[\frac{\Delta(s_{u,mob}/s_{u,av})}{\Delta(s_{u,max}/s_{u,av})}\right]^\zeta\right\}K_{max}$	(25)

stress, $\sigma'_v(\hat{x},\hat{z})$. This is represented by path A–B in the specific volume-vertical effective stress space (v-σ'_v) in Fig. 12. σ'_v moves towards the fully remoulded strength line (denoted RSL) at constant specific volume during undrained remoulding, causing accumulation of excess pore pressure, u_e (Fig. 11*d*). Maintained loads on the object will induce a total stress change and alter the equilibrium vertical effective stress, $\sigma'_{v,\,eqm}$, and generate additional excess pore pressure (Fig. 11*e*) that is either positive or negative depending on the loading direction and the location of the soil element relative to the object. During consolidation, excess pore pressure dissipation, $u_e(\hat{x},\hat{z})$, is calculated over the soil domain using a hyperbolic rate-form equation, and this change in excess pore pressure is used to update the current vertical effective stress, $\sigma'_v(\hat{x},\hat{z})$ (Fig. 11*f*). In v-σ'_v space, this is represented by the fully consolidated path B–C, first along the unload-reload line and then along the normal compression line (NCL) until the vertical effective stress equilibrates at $\sigma'_{v,\,eqm}$. The average undrained shear strength, $s_{u,\,av}$, mobilised by the object is calculated by a weighted average of the local undrained shear strength within the influence zone (Fig. 11*g*). The progressive mobilisation of $s_{u,\,mob}$ with displacement is considered using a nonlinear strength-displacement model (eq. 17), allowing the geotechnical capacity, q, to be calculated as $q = N_c s_{u,\,mob}$. The various equations associated with the preceding description are referred to in Fig. 11 and

Fig. 13. Idealised strain influence function: (*a*) plan view and (*b*) 3D view.

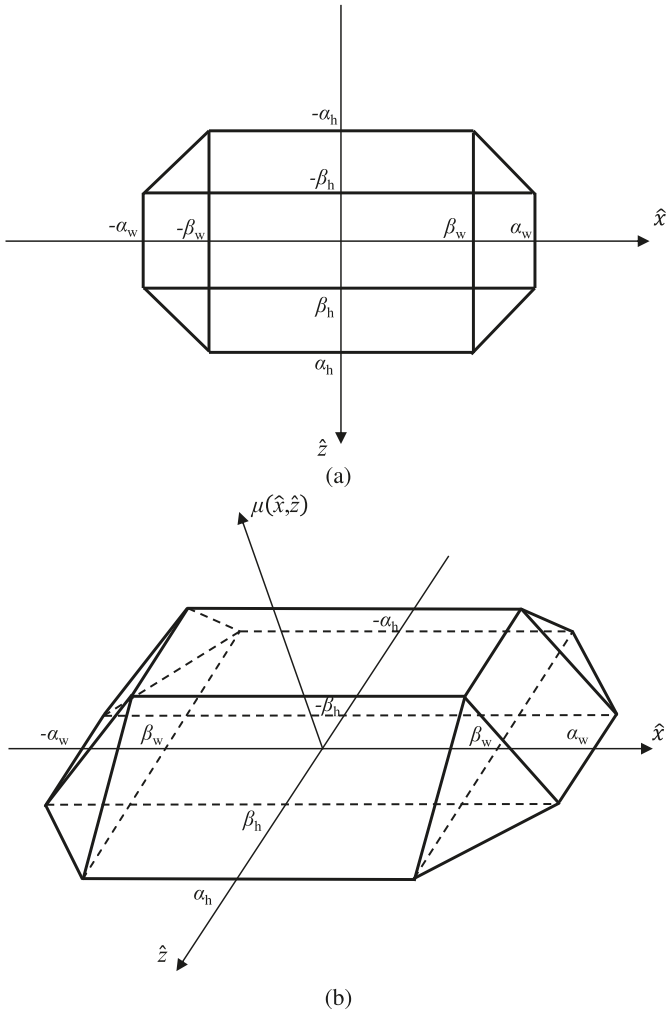

are listed in Table 2 (eqs. 10–25), or are detailed in the next section.

3.2. 2D framework extensions

The following sections provide details on the extensions and modifications to the framework; details on the original framework can be found in Zhou et al. (2019).

3.2.1. 2D strain and strength influence function

In the original effective-stress framework (Zhou et al. 2019), a simple probability density expression (i.e., $\int_{\hat{z}_c-\alpha}^{\hat{z}_c+\alpha} \mu(\hat{z})\,dz = 1$, where α is the vertical half extent of the 1D strain influence zone) is used to describe the distribution of incremental shear strain in a 1D discretised soil domain, where the strain influence function $\mu(\hat{z})$ was assumed to be triangular in distribution. This concept forms the basis for the 2D strain influence function $\mu(\hat{x},\hat{z})$ adopted here (as illustrated in Fig. 13), defined in a simple manner by four shape parameters, α_w, α_h, β_w, and β_h that satisfy $\int_{\hat{z}_c-\alpha_h}^{\hat{z}_c+\alpha_h}\int_{\hat{x}_c-\alpha_w}^{\hat{x}_c-\alpha_w} \mu(\hat{x},\hat{z})\,d\hat{x}d\hat{z} = 1$.

The piecewise-linear equation of the strain influence function can be expressed by

$$\text{(14a)}\quad \mu(\hat{x},\hat{z}) = h\begin{cases} 1, & |\hat{x}| \le \beta_w,\ |\hat{z}| \le \beta_h \\ 1-\dfrac{||\hat{z}|-\beta_h|}{\alpha_h-\beta_h}, & |\hat{x}| \le \beta_w,\ |\hat{z}| \ge \beta_h \\ 1-\dfrac{||\hat{x}|-\beta_h|}{\alpha_w-\beta_w}, & |\hat{x}| \ge \beta_w,\ |\hat{z}| \le \beta_h \\ 1-\dfrac{||\hat{z}|-\beta_h|}{\alpha_h-\beta_h}-\dfrac{||\hat{x}|-\beta_h|}{\alpha_w-\beta_w}, & |\hat{x}| \ge \beta_w,\ |\hat{z}| \ge \beta_h \end{cases}$$

where h denotes the height of the influence zone and is expressed by

$$\text{(14b)}\quad h = \frac{1}{4\beta_w\beta_h + 2\beta_w(\alpha_h-\beta_h) + 2\beta_h(\alpha_w-\beta_w) + \frac{2}{3}(\alpha_w-\beta_w)(\alpha_h-\beta_h)}$$

Specifically, α_w and α_h control the width (along the lateral direction, $\hat{x}$) and height (along the vertical direction, $\hat{z}$) of the influence zone, respectively, while β_w and β_h control the extent of the central plateau of the geometry. A particular advantage of adopting this form of $\mu(\hat{x},\hat{z})$, is that it provides a convenient and flexible means of adjusting the shear strain distribution for different foundation types.

Figure 14 compares the accumulated shear strain as quantified by the strain influence function, $\mu(\hat{x},\hat{z})$, with that calculated by the LDFE simulations for the cases of vertical penetration of a cylinder (case 1) and a circular plate (case 2). The best-fitted shape parameters for these cases are listed in Table 3. $\xi_{ref} = 9.21$ and 12.04 obtained from the LDFE results are taken for smooth and rough interfaces of case 1, respectively, representing the gross accumulated shear strain experienced by a given soil horizon for a full passage of an object into and out of the influence zone. As demonstrated earlier in the paper from the LDFE results for a circular plate, interface roughness only causes soil to become trapped above the plate (and to move with the plate) but has limited effect on the width of the influence zone (and more broadly the shape and extent of the failure mechanism) and the magnitude of strain accumulation within the influence zone. Consequently, $\xi_{ref} = 6.4$ (from the LDFE results for a smooth interface) is adopted in the framework for case 2 and is considered to be a lower bound on the accumulated shear strain.

The same integration scheme of accumulated shear strain (eqs. 4–5) is adopted to allow for a direct comparison between the strain influence function and the LDFE simulation. As shown in Figs. 14 and 15, the strain influence function provides close agreement with the LDFE results for the vertical distribution of accumulated shear strain with a smooth interface, whereas the agreement is poorer for the rough interface. The poorer agreement for the rough interface is because the form of the strain influence equations results in a steady state cumulative shear strain after sufficient displacement, whereas the LDFE simulated an increasing cumulative shear strain with increasing displacement due to the trapped soil moving downwards with the cylinder or plate, as discussed in the previous section.

For the lateral distributions of accumulated shear strain, there are evidently differences between the LDFE results and the strain influence function, due to the more complex vari-

Fig. 14. Comparison between large deformation finite element (LDFE) simulations and strain influence zone idealisations for case 1 (cylinder): (*a*) vertical profiles and (*b*) horizontal profiles.

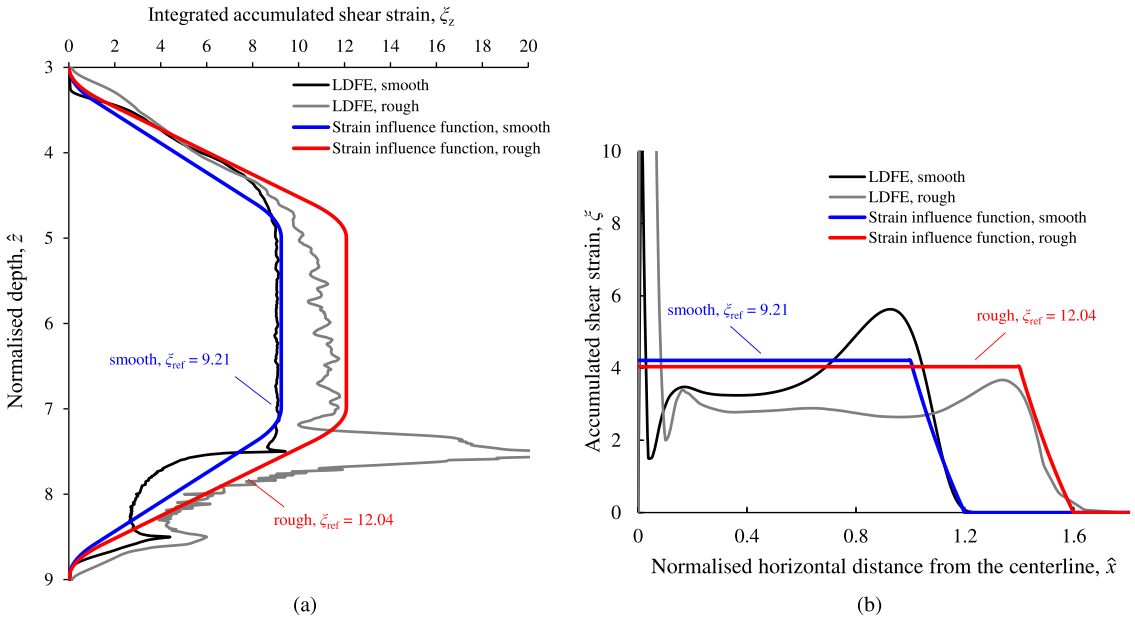

Table 3. Strain influence zone shape parameters.

	Interface	ξ_{ref}	α_w	α_h	β_w/α_w	β_h/α_h
Case 1 (cylinder)	Smooth	9.21	1.2	1.0	0.8	0.6
	Rough	12.04	1.6			
Case 2 (circular plate)	Smooth	6.4	1.0	0.5	0	0

ation in the lateral distributions that cannot be captured by a simple function. Nonetheless, the strain influence function is sufficiently flexible to model different distributions. For the cylinder (case 1, Fig. 14*b*), a large β_w ($\beta_w = 0.8\alpha_w$) is used to describe the evenly distributed shear strain in plane strain conditions, whereas $\beta_w = 0$ is needed to capture the sharp reduction in ξ from the centreline to the edge of the circular plate (Fig. 15*b*). Figure 15*b* also shows that the strain influence function (using $\xi_{ref} = 6.4$) provides excellent agreement with the LDFE results after a movement of around two diameters (i.e., by $\hat{z} = 6$) but underestimates $\bar{\xi}$ within a localised region just above the plate (Fig. 15*c*). As noted earlier, this localised increase from the LDFE results is due to trapped soil above the plate. However, the companion paper (Wang et al. 2024) shows that it is not necessary to replicate this behavioural aspect to replicate the response measured experimentally.

The average undrained shear strength, $s_{u,av}$, is also obtained by employing the weighted average concept via the strength influence function, $v_s(\hat{x}, \hat{z})$, which is of the same form as $\mu(\hat{x}, \hat{z})$, consistent with the work of Hodder et al. (2013) and Zhou et al. (2019).

3.2.2. Excess pore pressure due to a maintained load

In addition to the excess pore pressure induced by undrained shearing, additional excess pore pressure, $\Delta u_e(\hat{x}, \hat{z})$, is generated due to total stress changes when the foundation is subjected to a maintained load. Elastic solutions are commonly adopted to estimate the spatial distribution of $\Delta u_e(\hat{x}, \hat{z})$ (Cocjin et al. 2017; Corti et al. 2017; Zhou et al. 2019). In this study, the Zhou et al. (2019) expression to calculate the 1D distribution of excess pore pressure created by a maintained load is extended to a 2D domain and given as:

$$\Delta u_e(\hat{x}, \hat{z}) = \begin{cases} \left(\dfrac{1 - \text{sign}(v_p)}{2} - \eta\right)\left[\dfrac{6}{\pi}\iint_{\Re} Q(\mathbb{R})\dfrac{(\hat{z}_c - \hat{z})^3}{\left[4\hat{x}^2 + (\hat{z} - \hat{z}_c)^2\right]^{\frac{5}{2}}}d\mathbb{R}\right], \hat{z} < \hat{z}_c \\ \left(\dfrac{1 + \text{sign}(v_p)}{2} - \eta\right)\left[\dfrac{6}{\pi}\iint_{\Re} Q(\mathbb{R})\dfrac{(\hat{z} - \hat{z}_m)^3}{\left[4\hat{x}^2 + (\hat{z} - \hat{z}_c)^2\right]^{\frac{5}{2}}}d\mathbb{R}\right], \hat{z} \geq \hat{z}_c \end{cases} \quad (17)$$

Fig. 15. Comparison between large deformation finite element (LDFE) simulations and strain influence zone idealisations for case 2 (circular plate): (*a*) vertical profiles, (*b*) horizontal profile at depth of $\hat{z} = 6$, and (*c*) horizontal profiles within a localised zone at $\hat{z} = 8 \pm \Delta\hat{z}_{ext}$.

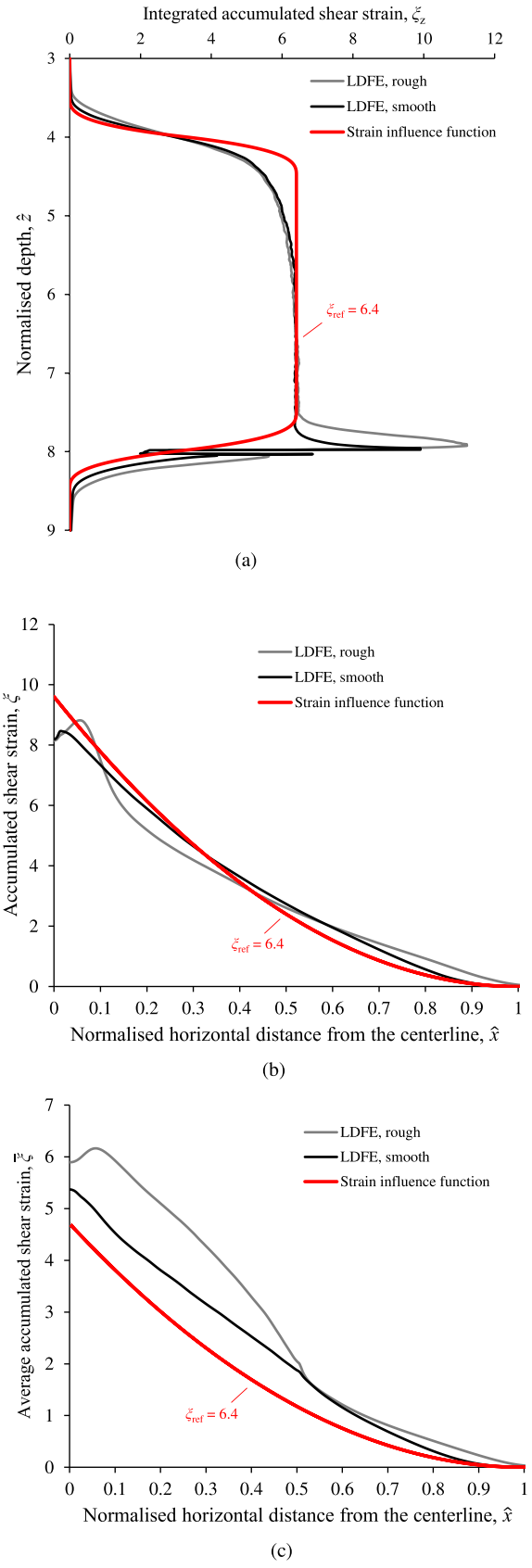

In eq. 17, the first bracketed term determines the direction of movements, whereas the second bracketed term calculates the stress distribution based on the elasticity approach for a circular loaded area, $\mathbb{R}$ (Poulos and Davis 1974). v_p is the object's penetration velocity, η controls the proportion of maintained load transferred into the soil either side of the object (η is in the range of 0–1, with $\eta = 0$ and 1 representing the cases where tensile stresses are zero and compressive stresses are zero, respectively; see Zhou et al. (2019) for further details), and Q ($\mathbb{R}$) denotes the superimposed pressure (i.e., from a combination of load components) exerted on the object, expressed as

$$(18) \quad Q = \sum_{i}^{N} Q_i, \; i = 1, 2, \ldots, N$$

where Q_i is the vertical contact stress induced by vertical, horizontal, or moment loading. This superposition principle has been adopted to calculate total stress changes in linear elastic soil (based on Poulos and Davis 1974) and is particularly advantageous when dealing with combined loading problems (Daivs and Selvadurai 1996).

The calculation of the current excess pore pressure using eqs. 16–18 allows the time-varying vertical effective stress to be determined for each soil element within the computational domain. The average undrained shear strength mobilised by the foundation can then be calculated by following the analysis procedure in Fig. 11, as demonstrated for various boundary value problems in the companion paper (Wang et al. 2024).

4. Concluding remarks

This paper extends the Zhou et al. (2019) effective stress framework, such that temporal and spatial distributions of soil strength due to undrained loading and reconsolidation can be calculated in a two-dimensional computational domain. The framework is built on critical-state concepts and links the generation of excess pore pressure to accumulated plastic shear strain. The consideration of boundary value problems within a 2D domain required accurate and applicable spatial distributions of plastic shear strain. These were established through large deformation finite-element simulations for the plane strain case of a deeply buried cylinder and the axisymmetric case of a deeply buried circular plate, considering both softening and non-softening soil responses.

A piecewise-linear form of a strain influence function, defined with sufficient generality to capture a variety of embedded foundation types, is shown to match well the average vertical and lateral distributions of shear strain accumulation produced in the finite element simulations. This strain influence function provides the basis for quantifying shear-induced excess pore pressure. Additional excess pore pressure induced by maintained loading is estimated using elastic solutions, and the dissipation of excess pore pressure was calculated using a rate form hyperbolic equation. These spatial and temporal changes in excess pore pressure allow the associated changes in undrained shear strength to be

calculated, which can be used in the framework to calculate capacity or resistance. The merit of the proposed framework is explored in the companion paper, where it is validated through a series of retrospective simulations of previously reported experimental data.

List of symbols

b	peak strength parameter
c_v	coefficient of consolidation
D	diameter
E	young's modulus
K	tangent stiffness
K_{max}	maximum tangent stiffness
m	parameter for dissipation rate
N_c	bearing capacity factor
$N_{c,\,i}$	bearing capacity factor for an ideal rigid-plastic material
$N_{c,\,s}$	softened bearing capacity factor
p	parameter for pore pressure generation rate
q	penetration resistance
$Q(\mathbb{R})$	superimposed vertical contact stress
Q_i	vertical contact stress induced by vertical, horizontal or moment loading
S_t	soil sensitivity
s_u	undrained shear strength
$s_{u,\,av}$	average undrained shear strength
$s_{u,\,i}$	in-situ undrained shear strength
$s_{u,\,mob}$	mobilised soil strength
s_{u0}	initial undrained shear strength
$(s_u/\sigma'_{v0})_{NC}$	normally consolidated undrained shear strength ratio
$\widehat{t}_p$	plate thickness
T	dimensionless time
t	time
T_{50}	dimensionless time required for 50% dissipation of the initial excess pore pressure
$u\,(\widehat{z})$	strain influence function (1D framework)
$u\,(\widehat{x},\widehat{z})$	strain influence function (2D framework)
u_e	excess pore pressure
v	specific volume
v_i	initial specific volume
v_p	penetration velocity
$v_s\,(\widehat{x},\widehat{z})$	strength influence function (2D framework)
$\widehat{w}$	normalised width of the disturbed zone
x	lateral distance
$\widehat{x}$	normalised lateral distance
$\widehat{x}_c$	horizontal coordinate (object centroid)
y	second axis of coordinate system
z	depth
$\widehat{z}$	normalised depth
$\widehat{z}_c$	vertical coordinate (object centroid)
α	extent of strain influence zone in the 1D framework
α_h	height of the influence zone
α_w	width of the influence zone
β_h	height of the central plateau in the influence zone
β_w	width of the central plateau in the influence zone
γ'	soil effective unit weight
$\dot{\gamma}_{max}$	maximum shear strain rate
Γ_{NCL}	specific volume, v, $\sigma'_v = 1$ kPa
δ_{rem}	inverse of soil sensitivity
$\Delta\widehat{z}_{ext}$	vertical above and below
$\dot{\varepsilon}_{max}$	principal strain rate
ζ	nonlinear tangent stiffness parameter
η	load sharing factor
κ	gradient of the unload-reload line (URL)
λ	gradient of the normal consolidation line (NCL)
$\mu(\widehat{x},\widehat{z})$	strain influence function
ξ	accumulated (absolute) plastic shear strain
ξ_0	initial strain
ξ_{95}	accumulated (absolute) shear strain a degree of remoulding 95%
$\xi_{95,\Phi}$	peak strength ductility parameter
ξ_p	average accumulated plastic shear strain
ξ_{ref}	reference accumulated plastic shear strain
ξ_x	integrated accumulated plastic shear strain within a local soil region along horizontal direction
ξ_z	integrated accumulated plastic shear strain along vertical direction
σ'_v	vertical effective stress
$\sigma'_{v,0}$	in situ geostatic effective stress
σ'_{vc}	pre-consolidation effective stress
$\sigma'_{v,\,eqm}$	equilibrium vertical effective stress
$\sigma'_{v,\,NCL}$	vertical effective stress on the NCL
$\sigma'_{v,\,RSL}$	vertical effective stress on the RSL
Φ	lumped strength parameter
Φ_{steady}	steady value of lumped strength parameter
χ	characteristic pressure

Acknowledgements

The work described in this paper was supported by the Australian Research Council through the Discovery Project research funding programme, ARC DP180103314. The third author acknowledges his research support from Norwegian Geotechnical Institute—NGI.

Article information

History dates

Received: 1 July 2022
Accepted: 8 August 2023
Accepted manuscript online: 29 November 2023
Version of record online: 1 May 2024

Notes

This paper is part one of two companion papers published in Canadian Geotechnical Journal. (Wang et al. 2024. Canadian Geotechnical Journal. doi:dx.doi.org/10.1139/cgj-2022-0332).

Data availability

Data generated or analysed during this study are available from the corresponding author upon reasonable request.

Author information

Author ORCIDs

C. D. O'Loughlin https://orcid.org/0000-0002-5823-6265
Z. Zhou https://orcid.org/0000-0002-3575-8810
C. Gaudin https://orcid.org/0000-0002-6326-4551

Author contributions

Conceptualization: YW, CDO, ZZ, CG
Formal analysis: YW, ZZ
Funding acquisition: CDO, CG
Investigation: YW, CDO, ZZ, CG
Methodology: YW, CDO, ZZ, CG
Project administration: CDO, CG
Resources: YW, CDO, ZZ, CG
Supervision: CDO, ZZ, CG
Validation: YW, CDO, ZZ, CG
Writing – original draft: YW, CDO, ZZ, CG
Writing – review & editing: CDO, ZZ, CG

Competing interests

The authors declare there are no competing interests.

References

Andersen, K.H. 2015. Cyclic soil parameters for offshore foundation design. 3rd ISSMGE McClelland Lecture. Frontiers in offshore geotechnics III, ISFOG'2015. Meyer, Taylor & Francis Group, London.

Bienen, B., and Cassidy, M.J. 2013. Set up and resulting punch-through risk of jack-up spudcans during installation. Journal of Geotechnical and Geoenvironmental Engineering, **139**(12): 2048–2059. doi:10.1061/(ASCE)GT.1943-5606.0000943.

Chow, S.H., O'Loughlin, C.D., and Zhou, Z. 2020. Penetrometer testing in a calcareous silt to explore changes in soil strength. Géotechnique, **70**(12): 1160–1173. doi:10.1680/jgeot.19.P.069.

Cocjin, M.L., Gourvenec, S.M., White, D.J., and Randolph, M.F. 2014. Tolerably mobile subsea foundations—observations of performance. Géotechnique, **64**(11): 895–909. doi:10.1680/geot.14.P.098.

Cocjin, M.L., Gourvenec, S.M., White, D.J., and Randolph, M.F. 2017. Theoretical framework for predicting the response of tolerably mobile subsea installations. Géotechnique, **67**(7): 608–620. doi:10.1680/jgeot.16.P.137.

Colreavy, C., O'Loughlin, C.D., and Randolph, M.F. 2016. Experience with a dual pore pressure element piezoball. International Journal of Physical Modelling in Geotechnics, **16**(3): 101–118. doi:10.1680/jphmg.15.00011.

Corti, R., Gourvenec, S.M., Randolph, M.F., and Diambra, A. 2017. Application of a memory surface model to predict whole-life settlements of a sliding foundation. Computers and Geotechnics, **88**: 152–163. doi:10.1016/j.compgeo.2017.03.014.

Dassault Systéms. 2014. ABAQUS 6.14 Analysis User's Manual. Simulia Corp, Providence, RI, USA.

Davis, R.O., and Selvadurai, A.P.S. 1996. Elasticity and geomechanics. Cambridge University Press.Cambridge, UK.

Einav, I., and Randolph, M.F. 2005. Combining upper bound and strain path methods for evaluating penetration resistance. International Journal for Numerical Methods in Engineering, **63**(14): 1991–2016. doi:10.1002/nme.1350.

Gan, C.T., Leung, C.F., Cassidy, M.J., Gaudin, C., and Chow, Y.K. 2012. Effect of time on spudcan–footprint interaction in clay. Géotechnique, **62**(5): 401–413. doi:10.1680/geot.10.P.063.

Gourvenec, S. 2020. Whole-life geotechnical design: what is it? What's it for? So what? And what next? Proceedings of the 4th International Symposium on Frontiers in Offshore Geotechnics (delayed to) 8–11 November 2021. *Edited by* Z. Westgate. Deep Foundations Institute, Austin, TX, USA. pp. 206–246.

Han, C., Wang, D., Gaudin, C., O'Loughlin, C.D., and Cassidy, M.J. 2016. Behaviour of vertically loaded plate anchors under sustained uplift. Géotechnique, **66**(8): 681–693. doi:10.1680/jgeot.15.P.232.

Hodder, M.S., White, D.J., and Cassidy, M.J. 2010. Analysis of soil strength degradation during episodes of cyclic loading, illustrated by the T-bar penetration test. International Journal of Geomechanics, **10**(3): 117–123. doi:10.1061/(ASCE)GM.1943-5622.0000041.

Hodder, M.S., White, D.J., and Cassidy, M.J. 2013. An effective stress framework for the variation in penetration resistance due to episodes of remoulding and reconsolidation. Géotechnique, **63**(1): 30–43. doi:10.1680/geot.9.P.145.

Hossain, M.S., and Randolph, M.F. 2009. New mechanism-based design approach for spudcan foundations on single layer clay. Journal of Geotechnical and Geoenvironmental Engineering, **135**(9): 1264–1274. doi:10.1061/(ASCE)GT.1943-5606.0000054.

Hu, Y., and Randolph, M.F. 1998. A practical numerical approach for large deformation problems in soil. International Journal for Numerical and Analytical Methods in Geomechanics, **22**(5): 327–350. doi:10.1002/(SICI)1096-9853(199805)22:5%3c327::AID-NAG920%3e3.0.CO;2-X.

Kong, V., Cassidy, M.J., and Gaudin, C.G. 2012. Failure mechanisms of a spudcan penetrating next to an existing footprint. Theoretical and Applied Mechanics Letters, **5**(2): 64–68. doi:10.1016/j.taml.2014.12.001.

Laham, N.I., Kwa, K.A., White, D.J., and Gourvenec, S.M. 2021. Episodic simple shear tests to measure strength changes for whole-life geotechnical design. Géotechnique Letters, **11**(1): 1. doi:10.1680/jgele.20.00124.

Martin, C.M., and Randolph, M.F. 2001. Applications of the lower and upper bound theorems of plasticity to collapse of circular foundations. *In* Proceedings of the 10th International Conference on Computer Methods and Advances in Geomechanics. Taylor & Francis, Abingdon, England. pp. 1417–1428.

Martin, C.M., and Randolph, M.F. 2006. Upper-bound analysis of lateral pile capacity in cohesive soil. Géotechnique, **56**(2): 141–145. doi:10.1680/geot.2006.56.2.141.

O'Loughlin, C.D., Zhou, Z., Stanier, S.A., and White, D.J. 2020. Load-controlled cyclic T-bar tests: a new method to assess effects of cyclic loading and consolidation. Géotechnique Letters, **10**(1): 7–15. doi:10.1680/jgele.19.00030.

O'Reilly, M.P., Stephen, F.B., and Robert, F.O., 1991. Cyclic loading of silty clay with drainage periods. Journal of Geotechnical Engineering, **117**(2): 354–362. doi:10.1061/(ASCE)0733-9410(1991)117:2(354).

Poulos, H.G., and Davis, E.H. 1974. Elastic solutions in soil and rock mechanics. Wiley, New York.

Purwana, O.A., Leung, C.F., Chow, Y.K., and Foo, K.S. 2005. Influence of base suction on extraction of jack-up spudcans. Géotechnique, **55**(10): 741–753. doi:10.1680/geot.2005.55.10.741.

Ragni, R., Wang, D., Mašín, D., Bienen, B., Cassidy, M.J., and Stanier, S.A. 2016. Numerical modelling of the effects of consolidation on jack-up spudcan penetration. Computers and Geotechnics, **78**: 25–37. doi:10.1016/j.compgeo.2016.05.002.

Randolph, M.F., and Andersen, K.H. 2006. Numerical analysis of T-bar penetration in soft clay. International Journal of Geomechanics, **6**(6): 411–420. doi:10.1061/(ASCE)1532-3641(2006)6:6(411).

Randolph, M.F., Low, H.E., and Zhou, H. 2007. In situ testing for design of pipeline and anchoring systems. *In* Offshore site investigation and geotechnics: confronting new challenges and sharing knowledge. Society of Underwater Technology.London, UK.

Randolph, M.F., White, D.J., and Yan, Y. 2012. Modelling the axial soil resistance on deep-water pipelines. Géotechnique, **62**(9): 837–846. doi:10.1680/geot.12.OG.010.

Roy, A., Chow, S.H., O'Loughlin, C.D., and Randolph, M.F. 2021. Towards a simple and reliable method for calculating uplift capacity of plate

anchors in sand. Canadian Geotechnical Journal, **58**(9): 1314–1333. doi:10.1139/cgj-2020-0280.

Sabetamal, H., Carter, J.P., Zhang, X., and Sheng, D. 2021. Coupled analysis of full flow penetration problems in soft sensitive clays. Computers and Geotechnics, **133**: 104054. doi:10.1016/j.compgeo.2021.104054.

Singh, V., Stanier, S., Bienen, B., and Randolph, M.F. 2021. Modelling the behaviour of sensitive clays experiencing large deformations using non-local regularisation techniques. Computers and Geotechnics, **133**: 104025. doi:10.1016/j.compgeo.2021.104025.

Sluys, L.J., and De Borst, R. 1992. Wave propagation and localization in a rate-dependent cracked medium—model formulation and one-dimensional examples. International Journal of Solids and Structures, **29**(23): 2945–2958. doi:10.1016/0020-7683(92)90151-I.

Song, Z., Hu, Y., and Randolph, M.F. 2008. Numerical simulation of vertical pullout of plate anchors in clay. Journal of Geotechnical and Geoenvironmental Engineering, **134**(6): 866–875. doi:10.1061/(ASCE)1090-0241(2008)134:6(866).

Sun, C., Feng, X., Bransby, M.F., Neubecker, S.R., Randolph, M.F., and Gourvenec, S. 2019. Numerical investigations of the effect of strain softening on the behaviour of embedded mooring chains. Applied Ocean Research, **92**: 101944. doi:10.1016/j.apor.2019.101944.

Tian, Y., Cassidy, M.J., Randolph, M.F., Wang, D., and Gaudin, C. 2014. A simple implementation of RITSS and its application in large deformation analysis. Computers and Geotechnics, **56**: 160–167. doi:10.1016/j.compgeo.2013.12.001.

Vulpe, C., Gourvenec, S., and Power, M. 2014. A generalised failure envelope for undrained capacity of circular shallow foundations under general loading. Géotechnique Letters, **4**(3): 187–196. doi:10.1680/geolett.14.00010.

Wang, Y. O'Loughlin, C.D. Zhou, Z. and Gaudin, C.G. 2024. A two-dimensional effective stress framework for modelling whole-life soil strength changes due to pore pressure generation and dissipation, Part 2: Applications. Canadian Geotechnical Journal . doi: https://doi.org/10.1139/cgj-2022-033

Wang, D., and O'Loughlin, C.D. 2014. Numerical study of pull-out capacities of dynamically embedded plate anchors. Canadian Geotechnical Journal, **51**(11): 1263–1272. doi:10.1139/cgj-2013-0485.

Wang, D., Hu, Y., and Randolph, M.F. 2010. Three-dimensional large deformation finite-element analysis of plate anchors in uniform clay. Journal of Geotechnical and Geoenvironmental Engineering, **136**(2): 355–365. doi:10.1061/(ASCE)GT.1943-5606.0000210.

White, D.J., and Hodder, M. 2010. A simple model for the effect on soil strength of episodes of remoulding and reconsolidation. Canadian Geotechnical Journal, **47**(7): 821–826. doi:10.1139/T09-137.

White, D.J., Doherty, J.P., Guevara, M., and Watson, P.G. 2022. A cyclic p-y model for the whole-life response of piles in soft clay, Computers and Geotechnics, **141**: 104519. doi:10.1016/j.compgeo.2021.104519.

Yap, Y.S., O'Loughlin, C.D., and Tom, J. 2020. A time-domain model for embedded and on-bottom chains incorporating consolidation. Proceedings of the 4th International Symposium on Frontiers in Offshore Geotechnics, Austin, USA.

Yasuhara, K., and Andersen, K.H. 1991) Recompression of normally consolidated clay after cyclic loading. Soils and Foundations, **31**(1): 83–94. doi:10.3208/sandf1972.31.83.

Zhang, Y., Bienen, B., Cassidy, M.J., and Gourvenec, S. 2012. Undrained bearing capacity of deeply buried flat circular footings under general loading. Journal of Geotechnical and Geoenvironmental Engineering, **138**(3): 385–397. doi:10.1061/(ASCE)GT.1943-5606.0000606.

Zhang, Y., Wang, D., Cassidy, M.J., and Bienen, B. 2014. Effect of installation on the bearing capacity of a spudcan under combined loading in soft clay. Journal of Geotechnical and Geoenvironmental Engineering, **140**(7): 04014029. doi:10.1061/(ASCE)GT.1943-5606.0001126.

Zhou, H., and Randolph, M.F. 2007. Computational techniques and shear band development for cylindrical and spherical penetrometers in strain-softening clay. International Journal of Geomechanics, **7**(4): 287–295. doi:10.1061/(ASCE)1532-3641(2007)7:4(287).

Zhou, Z., O'loughlin, C.D., and White, D.J. 2020b. An effective stress analysis for predicting the evolution of SCR–seabed stiffness accounting for consolidation. Géotechnique, **70**(5): 448–467. doi:10.1680/jgeot.18.P.313.

Zhou, Z., O'Loughlin, C.D., White, D.J., and Stanier, S.A. 2020c. Improvements in plate anchor capacity due to cyclic and maintained loads combined with consolidation. Géotechnique, **70**(8): 732–749. doi:10.1680/jgeot.19.TI.028.

Zhou, Z., White, D.J., and O'Loughlin, C.D. 2019. An effective stress framework for estimating penetration resistance accounting for changes in soil strength from maintained load, remoulding and reconsolidation. Géotechnique, **69**(1): 57–71. doi:10.1680/jgeot.17.P.217.

Zhou, Z., White, D.J., and O'Loughlin, C.D. 2020a. The changing strength of carbonate silt: parallel penetrometer and foundation tests with cyclic loading and reconsolidation periods. Canadian Geotechnical Journal, **57**(11): 1664–1683. doi:10.1139/cgj-2019-0066.